1-1-2012

Comparison Of Ceres-Modis Derived Polar Cloud Properties With Cloudsat/calipso And Ground-Based Measurements

Kathryn Giannecchini

COMPARISON OF CERES-MODIS DERIVED POLAR CLOUD PROPERTIES WITH CLOUDSAT/CALIPSO AND GROUND-BASED MEASUREMENTS

by

Kathryn Elyse Giannecchini
Bachelor of Science, Valparaiso University, 2009

A Thesis
Submitted to the Graduate Faculty

of the

University of North Dakota

in partial fulfillment of the requirements

for the degree of

Master of Science

Grand Forks, North Dakota
August
2012

This thesis, submitted by Kathryn Giannecchini in partial fulfillment of the requirements for the Degree of Master of Science from the University of North Dakota, has been read by the Faculty Advisory Committee under whom the work has been done, and is hereby approved.

Xiquan Dong

Baike Xi

Michael Poellot

This thesis is being submitted by the appointed advisory committee as having met all of the requirements of the Graduate School at the University of North Dakota and is hereby approved.

Wayne Swisher
Dean of the Graduate School

06-28-2012
Date

PERMISSION

Title Comparison of CERES-MODIS Polar Cloud Properties with CloudSat/ CALIPSO and Ground-Based Measurements

Department Atmospheric Sciences

Degree Master of Science

In presenting this thesis in partial fulfillment of the requirements for a graduate degree from the University of North Dakota, I agree that the library of this University shall make it freely available for inspection. I further agree that permission for extensive copying for scholarly purposes may be granted by the professor who supervised my thesis work or, in his absence, by the Chairperson of the department or the dean of the Graduate School. It is understood that any copying or publication or other use of this thesis or part thereof for financial gain shall not be allowed without my written permission. It is also understood that due recognition shall be given to me and to the University of North Dakota in any scholarly use which may be made of any material in my thesis.

Signature Kathryn Giannecchini

Date 06-28-2012

TABLE OF CONTENTS

LIST OF FIGURES

LIST OF TABLES

Table Page

ACKNOWLEDGEMENTS

I would like to first express my utmost appreciation to my advisor, Dr. Xiquan Dong, for his guidance, patience, enthusiasm, and for the skills that he has taught me through my three years as his student. In addition, I would also like to thank my advisory committee, Drs. Baike Xi and Mike Poellot, for their encouragement, understanding, and support in my research endeavors.

I would also like to extend my gratitude to the faculty, staff, and graduate students in the Atmospheric Sciences Department, as well as to the students in my research group, for their help with computer programming, stimulating discussions, and thought-provoking insight.

This study was primarily supported by the NASA CERES project at the University of North Dakota under Grant NNX10AI05G. To Drs. Patrick Minnis and Seiji Kato at NASA Langley Research Center: I would like to thank you for your questions and suggestions in regards to my research, as well as for the data you have provided (CERES-MODIS and CloudSat/CALIPSO).

Finally, achieving my goals would not have been possible without the loving support and encouragement I have received from my family and close friends. Thank you for believing in me and for always lending a helping hand.

ABSTRACT

Passive satellites often face difficulty when detecting clouds over snow and ice covered surfaces beneath them. The recent launches of active satellites, which directly measure cloud properties, have allowed scientists to gain a firsthand look at the complex cloud profiles across polar regions. To help quantify the differences between passive and active satellite retrievals, cloud properties derived for the Clouds and Earth's Radiant Energy System (CERES) project using MODerate Resolution Imaging Spectroradiometer (MODIS) data are compared with combined measurements from Cloud-Aerosol Lidar and Infrared Pathfinder Satellite Observation (CALIPSO) and CloudSat (CC), and Department of Energy (DOE) Atmospheric Radiation Measurement (ARM) observations at the North Slope of Alaska site, from July 2006 to June 2010. The study was then extended to include the entire Arctic and Antarctic.

During the 4-year period, monthly mean cloud fractions (CFs) between ARM and CC differ by 5%. While CERES-MODIS CF retrievals agree well with ARM and CC during warm months (May-October), retrievals during the cold season (November-April) significantly underestimate CF. Annual mean cloud-base heights derived from ARM and CC agree within 200 m, while their cloud-top heights (H_{top}) differ by an average of 1.2 km, due largely to CC detecting more upper-level clouds during the warm months. Effective cloud heights from CERES-MODIS retrievals fall between CC and ARM cloud bases and tops, as expected.

Cloud fractions and heights across the span of the Arctic depict similar features as those shown at the ARM NSA site. During summer months, cloud fractions between CERES-MODIS and CC agree well, differing by no more than 10% across most regions of the Arctic. During this same season, however, cloud heights vary by as much as 5.2 km. This is largely due to multi-layer cloud systems, where CC measures the uppermost cloud layer, and CERES-MODIS detects lower cloud layers, resulting in lower CERES-MODIS cloud heights, but equal cloud fractions. Winter shows a contrast to the similarities in cloud fraction detected in summer, with CERES-MODIS underestimating CF by as much as 59%. Cloud heights between the two platforms, however, show better agreement during the cold months, when fewer high clouds occur.

The largest differences in CERES-MODIS and CC cloud fractions and heights occur during the cold season (JJA) in the Antarctic. During this time period, CC detects cloud fractions as much as 43% higher than CERES-MODIS, over regions coupled with cloud heights up to 12.3 km higher than CERES-MODIS. These extreme differences are caused by the presence of polar stratospheric clouds, which occur at altitudes between 15 and 25 km, and are nearly impossible for the CERES-MODIS sensor to detect.

Finally, single-layered low-level stratus cloud effective radius (r_e), liquid water path (LWP), and optical depth (τ) retrieved from CERES-MODIS and surface-based retrievals at the ARM NSA site were investigated. When surface snow and sea ice are not present, ARM and CERES-MODIS retrieved cloud droplet r_e, LWP, and τ agree well. However, when snow and sea ice are introduced, CERES-MODIS retrieved r_e values are higher than ARM results, while optical depths are lower. These differences suggest that

CERES-MODIS cloud fraction retrieval algorithms during polar night and microphysical retrieval algorithms over snow and ice covered surfaces need future improvement.

CHAPTER I

INTRODUCTION

Clouds play an important and complex role in the radiative energy budgets of the Arctic and Antarctic. Factors such as low temperatures and moisture, reflective snow and ice surfaces, temperature inversions, and minimal solar radiation through a large portion of the year (Curry et al. 1996; Dong et al. 2010) contribute to the complexity of these cloud-radiative interactions in polar climates. Numerous studies have been performed in this area, including the First International Satellite Cloud Climatology Project (FIRE) Arctic Cloud Experiment (ACE; Curry et al. 2000), the Surface Heat Budget of the Arctic Ocean project (SHEBA; Uttal et al. 2002), and the South Pole Atmospheric Radiation and Cloud Lidar Experiment (SPARCLE; Walden et al. 2001). However, many questions remain in our understanding of the physical and dynamical processes of Arctic and Antarctic clouds.

While the Arctic and Antarctic are typically grouped together as "polar regions," their geographic and dynamic compositions are very different, leading to dissimilarities in satellite retrievals of cloud properties in these regions. The Arctic, for example, is essentially a large body of water surrounded by land. Alternatively, the Antarctic is composed of a large land mass surrounded on all sides by water. Despite their differences in land and ocean partitions, however, the Arctic and Antarctic are alike in that both are plagued by high amounts of surface snow and ice cover, which increase the complexity of the regions when passive satellites are used to detect cloud properties.

Additional dissimilarities lie in the cloud types that prevail over the two locations. Although both the Arctic and Antarctic experience a high frequency of low-level tropospheric clouds (Shupe et al. 2011; Adhikari et al. 2012), the occurrence of polar stratospheric clouds (PSCs) during polar night is much higher over the southern latitudes than in the north (Pitts et al. 2009; Adhikari et al. 2010). These clouds occur in two forms: Type I and Type II PSCs (Toon and Turco, 1991). Type I PSCs are nitric acid clouds, and are typically composed of nitric acid di- or trihydrate crystals (Type Ia; Voigt et al. 2000; Stetzer et al. 2006) or supercooled liquid ternary solutions (Type Ib; Carslaw et al. 1994), while Type II PSCs are ice clouds that consist of pure-water ice particles (Poole and McCormick 1988). PSCs typically form between 15 and 25 km in the atmosphere when temperatures are extremely cold (less than 200 K, Steel et al. 1983), allowing for the low amounts of water and nitric acid vapors in the stratosphere to condense onto stratospheric aerosols (Wang et al. 2008). These clouds play a key role in ozone depletion processes by acting as the catalysts for chemical reactions that destroy ozone (Toon and Turco, 1991; Pitts et al. 2007). Although PSCs have been documented in the Arctic (e.g. Santee et al. 2002, Cheremisin et al. 2007), the stratosphere rarely grows cold enough, and chemical transport is not sufficient enough to support PSC formation.

Minimal visual and thermal contrast exists between polar clouds and the snow- and ice-covered surfaces beneath them, which can lead to difficulties in passive satellite retrievals of cloud properties. This is especially true when visible and infrared wavelengths are used (Spangenberg et al. 2004; Curry et al. 1996). In addition, improvements to passive satellite cloud retrievals have been hindered by a lack of

available ground-based data in polar regions (Curry et al. 1996). The recent launches of satellites with on-board radar and lidar allow for direct measurements of cloud properties across both the North and South Poles and, when matched with available ground-based measurements, can provide a more complete picture of macrophysical cloud properties in polar regions.

The National Aeronautics and Space Administration (NASA) Clouds and Earth's Radiant Energy System (CERES) project was created to aid the understanding of global cloud-radiative interactions by simultaneously measuring cloud properties and radiation fields at the top of the atmosphere using instruments onboard several satellites (Wielicki et al. 1998; Minnis et al. 2011a). The goals of the CERES project are to provide global surface and top-of-atmosphere radiative fluxes with a higher accuracy than prior measurements, and to match these radiative fluxes with collocated cloud properties to create a climate data set valuable for investigating the role clouds play in the radiative balance of the climate system (Wielicki et al. 1996, 1998). These products are designed to improve understanding of cloud-radiation interactions and to help answer crucial climate questions.

The Cloud-Aerosol Lidar and Infrared Pathfinder Satellite Observation (CALIPSO) (Winker et al. 2007) and CloudSat (Stephens et al. 2002) satellites carry sensors designed to directly measure clouds and aerosols to provide vertical atmospheric profiles around the globe. Both satellites became operational in June 2006 as part of the NASA A-Train constellation of satellites (Winker et al. 2007; Stephens et al. 2008). When used properly, the cloud profiles produced by the CALIPSO Cloud-Aerosol Lidar with Orthogonal Polarization (CALIOP; Winker et al. 2007) and the CloudSat Cloud

Profiling Radar (CPR; Im et al. 2005) serve as a valuable data source to validate passive satellite retrievals (Kato et al. 2010). The CPR, which has a minimum detectible signal of -30 dBZ (Stephens et al. 2008), is unable to resolve low reflectivities, and therefore tends to miss some optically thin clouds. Alternatively, CALIOP is designed to detect optically thin clouds, but its signals are attenuated by optically thick clouds (Kato et al. 2010). When CPR and CALIOP observations are used together, the full spectrum of cloud types can be identified, providing a more complete global vertical cloud profile.

This study presents a comparison of cloud properties derived from MODerate resolution Imaging Spectroradiometer (MODIS) data for CERES with combined CALIPSO and CloudSat (CC) measurements from the CALIPSO-CloudSat-CERES-MODIS (CCCM) data set and ground-based observations taken at the Department of Energy (DOE) Atmospheric Radiation Measurement (ARM) program (Stokes and Schwartz, 1994) North Slope of Alaska (NSA) site (71.32°N, 156.62°W) near Barrow, AK. Cloud fractions and heights derived from all clouds are investigated from July 2006 through June 2010, while microphysical cloud properties are based on daytime low-level stratus clouds for June 2006 through December 2007 over the DOE ARM NSA site. Cloud microphysical properties, derived from both Terra and Aqua MODIS data using the NASA CERES Edition-2 algorithms (Minnis et al. 2011a) and denoted as CERES-MODIS data are compared with ground-based retrievals. Note that CERES uses different algorithms to retrieve MODIS cloud properties than those used by the MODIS Atmospheres Science Team (MOD06; Platnick et al., 2003). The differences are discussed by Minnis et al. (2011b). Surface and CC results are used to validate the

CERES cloud retrieval algorithms over open land and water, and over the complex snow and ice-covered terrains of the Arctic and Antarctic.

CHAPTER II

DATA SETS

The three data sets used in this study are: (1) Surface observations from the ARM NSA site, (2) CloudSat/CALIPSO combined cloud measurements, and (3) CERES-MODIS cloud property retrievals. CloudSat, CALIPSO, and Aqua, which houses the CERES and MODIS sensors, are all part of the A-train constellation of satellites. This line of sensors flies at an altitude of 705 km and passes the equator at 1:30 PM local standard time. Retrievals from the ARM NSA site are used as a ground truth to validate the satellite cloud products. Details regarding these data sets are provided below.

Surface Observations

At the Department of Energy (DOE) Atmospheric Radiation Measurements (ARM) North Slope of Alaska (NSA) site, cloud data are measured by several active, ground-based sensors, including the millimeter wavelength cloud radar (MMCR; Moran et al. 1998), the micropulse lidar (MPL), and the Vaisala ceilometer. The MMCR is a vertically-pointed radar that operates at a wavelength of 8.6 mm. It is able to provide continuous radar reflectivity profiles by sending pulses of energy into the atmosphere and collecting the energy scattered back to the transceiver by hydrometeors moving through the radar field of view. These profiles are reported at a vertical resolution of 45 m and allow for the identification of both cloudy and clear conditions at the ARM sites. The MPL sends and receives pulses of energy in a manner similar to that of the MMCR, but uses a wavelength of 532 nm and reports cloud properties at a vertical resolution of 30 m.

The ceilometer sends out near-infrared pulses of light, which are scattered back from clouds and precipitation, allowing for the detection of clouds below a height of 7.7 km with 10 m vertical resolution. Cloud property data are only included when all three instruments are in working order.

The different sensitivities of the three instruments used for ARM NSA cloud property retrievals allow for a more accurate depiction of cloud heights and cloud fraction for the region. The MMCR, which is sensitive to the sixth moment of the cloud particle distribution, is more sensitive to insects and drizzle or rain drops below the cloud base than either the MPL or ceilometer, rendering it difficult for the MMCR alone to consistently retrieve accurate cloud base heights. However, the MPL and laser ceilometer are sensitive to the second moment of the cloud particle distribution, causing them to be more adept for retrieving cloud bases than the MMCR. The MPL is also more sensitive to optically thin clouds, which allows for the detection of high, thin cirrus clouds that might remain undetected by both the MMCR and laser ceilometer. Consequently, many studies have combined radar and lidar measurements to estimate cloud fraction and boundaries (e.g. Intrieri et al. 2002; Dong et al. 2005, 2010).

Cloud fraction is defined as the ratio of the number of samples where the radar, lidar, or ceilometer have detected clouds to the total number of samples when data are available from all three instruments within a specified time period. For the purposes of this study, cloud fraction, highest cloud-top heights, and lowest cloud-base heights are from the Active Remote Sensing of Clouds (ARSCL) products (Clothiaux et al. 2000). The ARSCL products use data derived from a blend of MMCR reflectivities, which have the ability to clearly define the highest cloud-top heights, and MPL- and ceilometer-

derived lowest cloud-base heights, which are more sensitive to smaller cloud particles and cloud bases. Each parameter is reported at 45 m vertical intervals when the MMCR, MPL, and ceilometer are all in operation. During December of 2006 and 2007, as well as January of 2007, MMCR faults at the ARM NSA site prevented measurements of macrophysical cloud properties. Therefore, these three months are not included in monthly averages of cloud fraction or heights in this study. Cloud liquid water path (LWP) is derived from microwave radiometer brightness temperatures at 23.8 and 31.4 GHz using the statistical retrieval method described by Liljegren et al. (2001). Using this method, the root-mean-square (RMS) accuracies of the LWP retrievals are approximately 20 gm^{-2} for cloud LWP below 200 gm^{-2} and 10% for LWP exceeding 200 gm^{-2} (Dong et al. 2000; Liljegren et al. 2001).

To retrieve the microphysical properties of single-layered stratus clouds, the approach taken by Dong et al. (1998) was used, with a modification to include surface albedo introduced by Dong and Mace (2003). In this approach, a δ2-stream radiative transfer model was used with the input of ground-based measurements to retrieve layer-averaged microphysical properties of single-layered low-level stratus clouds. This scheme is based on an iterative approach in which the effective radius is varied in radiative transfer calculations until the solar transmission calculated by the model matches the observations. From these calculations, layer-mean cloud-droplet effective radius (r_e), number concentration (N), broadband shortwave optical depth (τ), and albedos at the top of the cloud (R_{cld}) were retrieved (Dong et al. 1998). The retrieved r_e and radiative properties were then parameterized as functions of the cloud LWP, effective solar transmission (γ), cosine of the solar zenith angle (μ_0), and surface albedo (R_{sfc}) as

described by Dong and Mace (2003). Compared to aircraft in situ measurements over the mid-latitudes, the uncertainties of the surface-retrieved r_e, τ, and LWP values under snow and ice-free conditions are approximately 10% (Dong et al. 1998, 2002). Over the snow and ice covered surfaces, the uncertainties of the surface retrievals are at least doubled as compared to the aircraft in situ measurements during FIRE-ACE in May 1998 (Dong et al. 2001), and to other aircraft in situ measurements near the ARM NSA site as discussed in Section 4d of Dong and Mace (2003).

Satellite Measurements

CloudSat/CALIPSO (CC)

In order to develop a more thorough understanding of the cloud properties at the ARM NSA site, as well as across the Arctic and Antarctic, active space borne sensors are also used. One such sensor, the CloudSat Cloud Profiling Radar (CPR), is a 94-GHz nadir-viewing radar that measures the amount of power backscattered by clouds to create a vertical profile of cloud structure around the globe (Im et al. 2005). Alternatively, the Cloud-Aerosol Lidar with Orthogonal Polarization (CALIOP) onboard the Cloud-Aerosol Lidar and Infrared Pathfinder Satellite Observation (CALIPSO; Winker et al. 2007), is a nadir-pointing polarization-sensitive lidar operating at wavelengths of 1064 and 532 nm to provide vertical profiles of aerosols and clouds (Winker et al. 2007).

The CloudSat and CALIPSO cloud properties used in this study are from the CALIPSO-CloudSat-CERES-MODIS (CCCM) RelB1 data product. In this dataset, the CALIPSO Vertical Feature Mask (VFM; Version 3) and CloudSat Level 2B Cloud Scenario Classification (CLDCLASS; Revision 4) products are merged and combined with CERES-MODIS data to build a comprehensive dataset that includes atmospheric

profiles of clouds and aerosols from CALIOP and CPR, in addition to cloud properties derived from MODIS radiances using the CERES-Edition-3 beta-2 cloud algorithm (Kato et al. 2010).

The CloudSat CLDCLASS product, which is based on CPR reflectivity, offers a cloud mask that provides information at resolutions of 1.4 km cross-track, 1.8 km along-track, and 240 m vertically (Stephens et al. 2008). The cloud and aerosol mask provided by the VFM, however, offers a horizontal resolution of 333 m, with a vertical resolution of 30 m below 8.2 km and 60 m above (Winker et al. 2007). To account for the differences in horizontal resolutions, one profile from the CloudSat CLDCLASS product is combined with three CALIPSO VFM profiles to produce a single profile with a horizontal resolution of 1 km. During the merging process, cloud boundaries from the CPR are added to CALIOP-derived cloud profiles if the CPR detects a boundary more than 480 m above or below CALIOP-derived heights, or if the CALIOP signal is attenuated in its entirety by clouds and the CPR-derived cloud base is located beneath the level of attenuation. Otherwise, the level of CALIOP attenuation is reported as the cloud base (Kato et al. 2010). As a result, approximately 85% of cloud-top heights and 77% of cloud-base heights within the merged profiles are reported by CALIOP (Kato et al. 2010).

After CloudSat and CALIPSO cloud profiles have been merged, they are collocated with CERES footprints that are roughly 20 km in size. The 1-km atmospheric columns that contain similar cloud vertical profiles are then arranged together in a cloud grouping process. After similar cloud profiles have been grouped together, the cloud fraction of each group is computed for times when both the CPR and CALIOP are in

operation, and then summed to produce the mean cloud fraction along the ground track for a given pixel (Kato et al. 2010).

In addition to merged profiles that allow for measurement of cloud fraction and heights, the CCCM data set also includes cloud microphysical properties, including cloud-droplet effective radius, retrieved from the CloudSat radar reflectivity. These properties are derived from the CloudSat Level 2B Cloud Water Content Radar Only (CWC-RO; Revision 4) product. The CWC-RO uses measured radar reflectivity as the only input to create composite profiles from both ice and liquid water retrievals. For each profile, CWC-RO algorithms first examine cloud masks to determine which bins contain clouds, and then use the 2B-CLDCLASS product to eliminate any invalid or undetermined cloud types. Once valid cloud profiles have been retrieved, a priori values are assigned to particle size distribution parameters within each cloudy bin based on factors such as climatology and temperature. A priori values and radar measurements are then used to retrieve liquid and ice particle size distribution parameters for each cloudy bin, allowing for the derivation of r_e.

CERES-MODIS

The MODerate Resolution Imaging Spectroradiometer (MODIS) sensor, which is on board the Aqua and Terra satellites, has a swath width of 2,330 km and provides global coverage of cloud and aerosol properties. The CCCM data product provides Aqua FM3 (Edition 3, beta 2; Minnis et al. 2010) cloud properties within pixels limited to the region covering the CloudSat/CALIPSO swath, instead of using the wide footprint of a full MODIS sweep. These data are used for the cloud height and cloud fraction analyses. Cloud microphysical parameters, however, are derived from Terra Edition2B and

Edition2G products, in addition to Aqua Edition2B and Edition2C products, and include the full CERES-MODIS swath to increase the number of cases available.

CERES-MODIS cloud properties were computed from the CERES Single Scanner Footprint (SSF) product. The SSF combines CERES 20-km resolution broadband flux measurements with concurrent 1-km MODIS cloud and aerosol retrievals. The MODIS pixels are classified as either cloudy or clear based on a cloud mask for polar regions (Trepte et al. 2002) that utilizes the 0.64, 2.13, 3.78, 10.8, and 12.0 μm MODIS channels. Clear and cloudy pixels are categorized as either weak or strong to denote the degree of confidence in the classification. Pixels categorized as cloudy are analyzed to derive a series of cloud properties that include cloud phase, effective cloud temperature (T_{eff}), and effective cloud height (H_{eff}), r_e, τ, and LWP or ice water path (IWP).

Several retrieval methods are used by CERES to derive cloud information from MODIS data. During daytime conditions, when the solar zenith angle is less than 82º, cloud properties are retrieved using the 4-channel visible-infrared shortwave-infrared split-window technique (VISST). The VISST employs the visible (0.63 μm) channel to estimate τ, the shortwave-infrared (3.7 μm) band to retrieve r_e, the infrared (10.8 μm) channel to estimate T_{eff}, and the split-window (12 μm) band to aid in thermodynamic phase identification. Because of the high surface albedos at the 0.63-μm channel for snow and ice-covered scenes, the shortwave-infrared infrared near-infrared technique (SINT) introduced by Platnick et al. (2001) is used when surface snow and ice are present. The SINT takes advantage of the small snow and ice albedos at some near-infrared wavelengths, and is essentially the same as the VISST, except that the 1.6-μm

(Terra) or 2.1-μm (Aqua) channel is used instead of the visible channel to estimate τ. The Aqua analyses used the 2.1-μm channel because its 1.6-μm channel was malfunctioning. This algorithm is used whenever either the scene classification from neighboring clear pixels or snow and ice maps from the CERES data stream identify the background surface as snow or ice-covered. During nighttime, when the solar zenith angle exceeds 82º, the solar-infrared infrared split-window technique (SIST) is used. The SIST uses the 3.7-, 10.8-, and 12-μm channels to retrieve the same parameters as the VISST, except that the useful information at these wavelengths is generally limited to clouds having an optical depth less than 10 (Minnis et al. 2011a).

The CERES-MODIS H_{eff} is determined from T_{eff} by matching it with a modified numerical weather analysis (NWA) of the vertical temperature profile. The lower half of the NWA profile is replaced with temperatures computed using a 7.1ºC km^{-1} lapse rate anchored to the 24-hour mean surface air temperature (Dong et al. 2008) or sea surface temperature. Details of the lapse rate modification are provided by Minnis et al. (2011a). Cloud LWP is then calculated by combining the retrieved τ and r_e in the equation

$$LWP = \frac{2}{3}\rho_l \tau r_e \quad (1)$$

where ρ_l is the density of liquid water, τ is optical depth, and r_e is effective radius.

CHAPTER III

METHODOLOGY

Satellite Spatial Analysis at Barrow Site

When comparing surface and satellite observations, the surface radar/lidar field of view is much smaller than the satellite fields of view, resulting in spatial and temporal differences between ground-based and space-borne observations. While the instruments at the ARM NSA site can provide many profiles of cloud information per hour, the polar orbiting nature of the satellites and narrow swath widths of the CPR and CALIOP prevent the satellites from taking instantaneous observations directly over the ARM site more than two to three times per month. To match the temporal and spatial scales as closely as possible for the surface-satellite comparison, the overpass frequency, which is defined as the percentage of satellite overpasses per month, of the space-borne radar/lidar was first taken into consideration.

As Figure 1 shows, increasing the size of the grid box centered on the ARM NSA site from 1ºx1º to 7ºx7º increases the overpass frequency from approximately 20%, where CloudSat/CALIPSO (CC) data were available approximately six times per month, to 100%. At the 3ºx3º grid box, the cloud fraction percentage begins to stabilize, indicating that there are enough samples to produce consistent results. At this same point, the overpass frequency climbs to 60%, which translates to approximately 18 samples per month each year, and 72 total samples per month during the 4-year period in this study. From this, we conclude that the use of a 3ºx3º grid box area can provide a sufficient

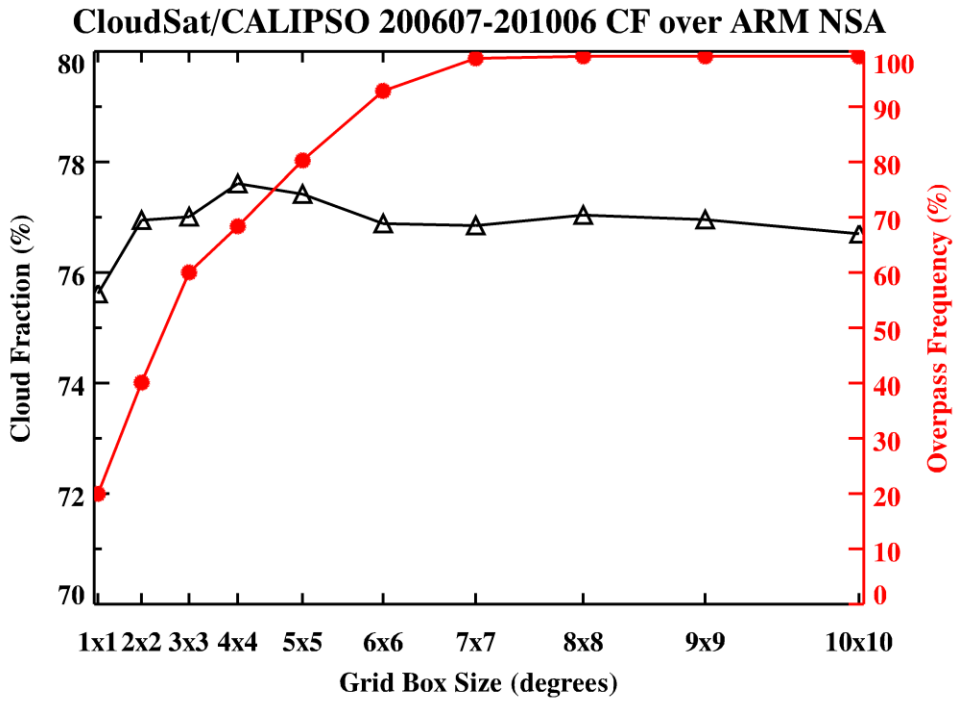

Figure 1. CloudSat/CALIPSO cloud fraction (black triangles) and overpass frequency (red circles) with increasing grid box size around the ARM NSA site in Barrow, AK.

Figure 2. Reference map of Arctic locations.

number of CC samples for this study. As a result, all macrophysical cloud properties from satellite data in this study are averaged within a 3ºx3º area (333 km latitude by 115 km longitude) centered on the ARM NSA site near Barrow, AK, while microphysical properties are averaged within a 1°x3° area (111 km latitude by 115 km longitude). Because the NSA site is located on the north Alaska coast, as demonstrated by the blue asterisk in Figure 2, the surface of the comparison region is roughly half ocean and half land.

Satellite Evaluation in Polar Regions

The use of data from sensors included in the A-train constellation of satellites ensures that all satellite retrievals cover the same time period. The active sensors, CloudSat and CALIPSO, trail Aqua by 60 and 75 seconds, respectively. As a result, all satellite measurements are collocated in both time and space. These measurements are then averaged into grid boxes of 3ºx3º across the span of the Arctic and Antarctic.

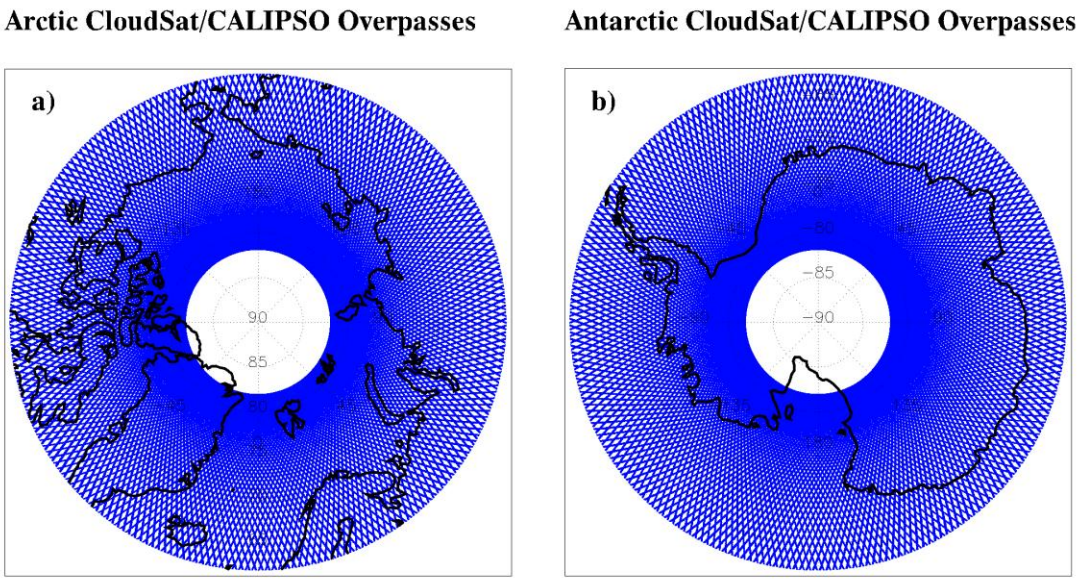

Figure 3. CloudSat/CALIPSO overpasses over (a) the Arctic, and (b) the Antarctic, from July 2006 to June 2010.

Although CloudSat and CALIPSO are polar-orbiting satellites, the widths of their swaths are so narrow that regions closest to the poles remain unsampled, as shown in Figure 3, which documents the locations of all overpasses made by CloudSat and CALIPSO between July 2006 and June 2010. Due to the lack of available data, the Arctic is defined as the region covering all longitudes between 61.5ºN and 82.5ºN in this study. Similarly, the Antarctic is represented by all longitudes between 61.5ºS and 82.5ºS.

Another complication that occurs when using data from high latitudes stems from the sizes of grid boxes used for averaging. The polar regions experience a narrowing of longitudinal area closest to the poles. As a consequence, the size of the 3ºx3º grid boxes across the focus areas range from 333 km latitude by 52 km longitude closest to 82.5ºN/S, to 333 km latitude by 152 km longitude nearest to 61.5ºN/S. To account for these large spatial differences, Arctic- and Antarctic-wide averages are weighted by grid box size using the equation

$$Average = \frac{\sum d*w}{\sum w} \qquad (2)$$

where *d* represents the data being averaged (i.e. cloud fraction, cloud-top height, etc.) and *w* is the weighting function, which is equivalent to the area of the grid box.

Selection of Single Layer Stratus Cases at ARM NSA Site

Initial efforts to select daytime single-layered low-level stratus clouds from ARM and CERES-MODIS retrievals at the ARM NSA site identified a total of 477 Terra cases, and 557 cases from Aqua, between July 2006 and December 2007. Further examination of satellite and radar imagery was then used to screen the data and remove instances that included multiple stratus cloud layers and overlying cirrus. This process reduced the

number of daytime low-level stratus cases to 365 and 413 for Terra and Aqua, respectively. To investigate the potential effects of surface and snow cover, the data sets were also separated by ground cover composition. Dong et al. (2003, 2010) found surface albedo at the ARM NSA site to equal ~0.2 under bare ground conditions. Therefore, it is assumed that the ground was bare if the ARM-derived surface albedo was less than 0.2, and snow and ice cover were present if the surface albedo exceeded 0.2. Because only observations having solar zenith angles less than 82º were considered, months with surface albedo higher than 0.2 ranged from October to June, but excluded days influenced by polar night from November through February. This separation divided the total number of cases into 113 with surface snow cover and 252 without for Terra, and 147 with snow cover and 266 without for Aqua.

CHAPTER IV

RESULTS AND DISCUSSION

PART 1: Comparison of Cloud Macrophysical Properties at ARM NSA Site

Comparisons of cloud macrophysical properties have been conducted over the ARM NSA site in Barrow, Alaska. Cloud fractions and cloud heights derived from the CloudSat/CALIPSO radar-lidar and CERES-MODIS observations are compared with combined MMCR, MPL, and ceilometer observations at the ARM NSA site in Barrow, AK, from July 2006 to June 2010.

Cloud Fraction

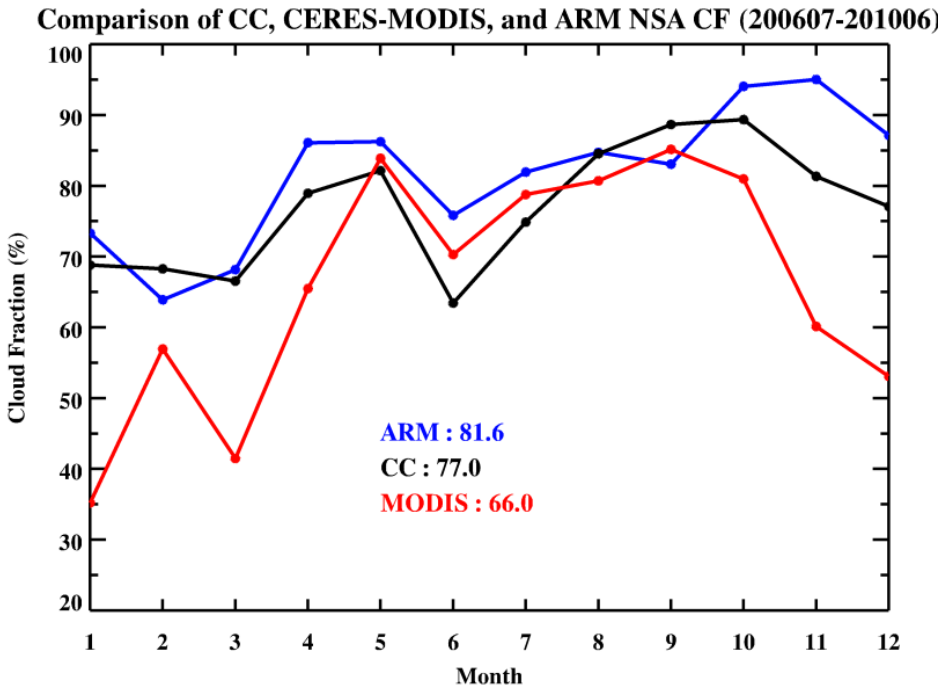

Figure 4. Monthly mean cloud fractions derived from CloudSat/CALIPSO (black), CERES-MODIS (red), and ARM radar-lidar (blue) over the ARM NSA site from July 2006 to June 2010.

As demonstrated in Figure 4, the monthly mean cloud fraction (CF) from the ARM NSA instruments increases from March through May (68% to 86%), decreases from May to June (86% to 76%), then rises to a secondary maximum in November (95%) before decreasing again through winter. The 4-year mean of CF from the ARM instruments averages to 81.6%, which is comparable to the annual average of 78% determined by Dong et al. (2010) in a study of ARM NSA radar-lidar CFs from 1998-2004.

Cloud fractions from CC follow a similar pattern to ARM results, increasing to an early spring maximum (82%) before subsequently decreasing in June (63%), then rising to a second peak in October (89%), with an annual average of 77%. This same general trend is evident in CERES-MODIS results, with warm month (May through September) averages (80%) agreeing within 5% of ARM (85%) and CC (81%). During the cold season from October to April, however, CERES-MODIS estimated CFs are much lower than those derived from ARM and CC, with the largest difference in December-January. The CERES-MODIS annual average is 66% during the 4-year period, which is 11% lower than CC and 15.6% lower than ARM.

Cloud Heights

Figure 5 shows the monthly mean highest cloud-top (H_{top}) and lowest cloud-base (H_{base}) heights observed by ARM and CC radar-lidar combinations, and cloud effective height (H_{eff}) derived from CERES-MODIS over the ARM NSA site. Monthly means of H_{base} measured by ARM and CC agree well, with annual averages (±standard deviation) of 1.3±1.9 and 1.1±1.4 km, respectively, and mean differences ranging from roughly 0.15 km in August to 0.8 km in February. The monthly means of H_{top} from ARM and CC also

agree well through the winter and early spring months, averaging to 4.3 and 4.7 km, respectively, between November and April. After April, however, the similarities in H_{top} begin to deviate. While CC H_{top} begins a steady increase through the early summer, ARM H_{top} levels off or slightly decreases, until a maximum difference (4 km) is reached between the two in September. To investigate these warm season discrepancies, the PDF and CDF of the highest cloud-top heights derived from ARM and CC are plotted at 500 m intervals for all months (Figure 6a), March (Figure 6b), and August-September (Figure 6c).

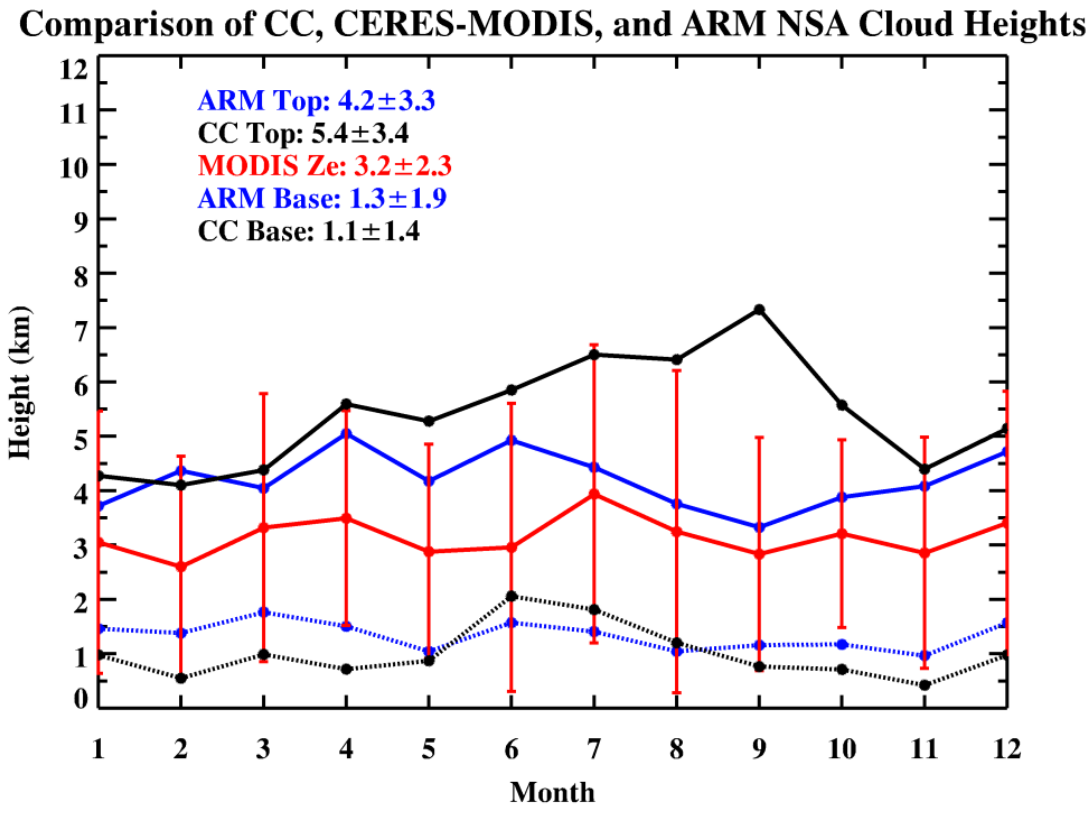

Figure 5. Monthly means of highest cloud-top (solid) and lowest cloud–base (dashed) heights derived from ARM NSA radar-MPL-ceilometer measurements (blue), CloudSat/CALIPSO observations, and CERES-MODIS effective cloud height (red with standard deviation) from July 2006 to June 2010.

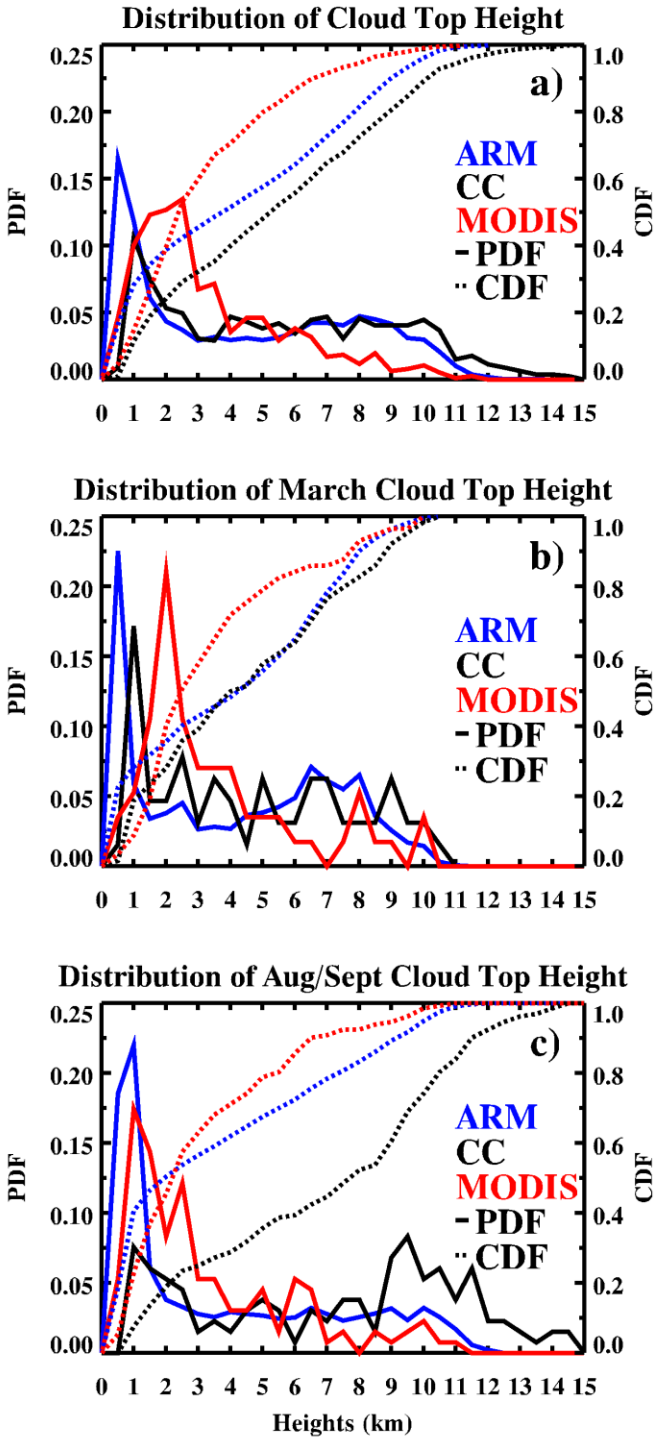

Figure 6. Vertical distributions of highest cloud-top height for ARM (blue), CC (black), and CERES-MODIS (red) for (a) July 2006 through June 2010, (b) March, and (c) August-September. Solid lines represent the probability density function (PDF) of highest cloud-top heights, while dashed lines show the cumulative distribution function (CDF).

Throughout the year, the ARM and CC PDFs and CDFs vary. Figure 6b illustrates that, during March, the ARM and CC PDFs and CDFs are nearly identical at altitudes above 1 km, resulting in the similar monthly means of highest cloud-top heights seen in Figure 5. During August-September, however, the PDFs and CDFs differ significantly. Both ARM and CC show peaks in cloud occurrence at 1 km. However, the CDFs show that the ARM radar-lidar observed approximately 40% of clouds by this altitude, while CC only measured 8% of total clouds below 1 km.

Discussion

There are several potential reasons that lead to the 5% difference between ARM and CC cloud fraction, including spatial and temporal mismatches between the space- and ground-based radar-lidar observations and their different sensitivities and/or fields of view of clouds. As demonstrated in Figure 6a, the ARM radar-lidar detected more (25% of total clouds) low-level clouds (cloud-top heights below 1 km) than CC (10%). This result indicates that the 6% CF difference in Figure 4 is most likely due to CC measurement limitations in detecting clouds below 1 km.

During a study of radar-lidar CFs at the ARM NSA site, Dong et al. (2010) found that the annual CF was 78% from radar-lidar measurements during the period 1998-2004, which is comparable to the 4-year averages determined by the ARM and CC radar-lidar combinations in this study. However, the CERES-MODIS CF is only 66%, with the largest underestimates found during the cold months (November-April). The monthly differences are similar to those found by Kato et al. (2006) between the ARM lidar and CERES-MODIS cloud amounts over the NSA site from March 2000 through February 2004. In that study, the lidar-determined mean cloud fraction was 74% for the 4-year

period, compared to 71% from the CERES-MODIS. Kato et al. (2006) also found that the cloud fraction over the NSA site determined using only radar data was only 57%, indicating that many of the clouds are very thin or tenuous.

During the cold months, the CERES-MODIS retrieved CFs are much lower than those derived from the active radar-lidar observations of ARM and CC. ARM radar-lidar images (not shown) reveal that the clouds appearing over Barrow tend to be physically thin and closer to the ground during the cold months. It has been documented that CERES-MODIS has a tendency to miss clouds with optical thicknesses less than 0.3 (Chiriaco et al. 2007; Minnis et al. 2008), which may account for some of the differences in Figure 4. During the cold months, the land and sea surrounding Barrow are typically covered by snow and ice, mostly in darkness, and very cold. Thus, only infrared channels are used in the mask, which have difficulty detecting thin clouds in nearly isothermal conditions that produce small, often unambiguous signals, particularly at low altitudes, where the atmosphere is often warmer than the surface.

From May through September, however, CFs derived from the three platforms agree within 5%, ranging from 85% for the ARM radar-lidar, to 81% for CC, and 80% for CERES-MODIS. Since the Arctic experiences nearly 24 hours of daylight during summer months, data are taken mostly in daylight during those months. The visible contrast between clouds and background in snow-free conditions and the shortwave-infrared and near-infrared contrast for snow-covered scenes along greater cloud-surface thermal contrast facilitate more accurate detection of clouds by CERES-MODIS sensors during that time period. Only the thinnest or smallest clouds are missed by MODIS sensors during that time period.

When comparing cloud heights, it must first be known that H_{eff} is converted from a measure of the brightness temperature, T_{eff}, representing cloud radiative center. It was expected that H_{eff} would fall between ARM and CC radar-lidar measured H_{top} and H_{base} values. As discussed in Dong et al. (2008), H_{eff} is generally close to H_{top} for optically thick clouds and nearer to the cloud center or H_{base} for optically thin clouds. According to Minnis et al. (2008), H_{eff} should represent an optical depth of ~1.1 down from the cloud top, which corresponds to 1-2 km in ice clouds, even in optically thick ice clouds, but much less in liquid water clouds (~0.5 km in Dong et al. 2008). This depth is consistent with the results in Figure 5, where monthly means and standard deviations of H_{eff} basically fall within the cloud boundaries of ARM and CC measurements, with an annual average of 3.2±2.3 km and are 1-2 km below the ARM and CC tops.

As demonstrated in Figure 5, monthly means of H_{eff} range from as low as 2.6 km in February to 3.9 km in July, and are very close to ARM H_{top} values from July to September. Further investigation of cloud type using cloud radar imagery from ARM NSA throughout the 4-year period showed that, during this time period, the Barrow site tended to experience the highest frequency of both optically thick convective clouds and multi-layered clouds, where optically thin high-level clouds occur over lower clouds, than other seasons. In optically thick convective clouds, the radiative centers are higher in the atmosphere and their corresponding H_{eff} values are reported closer to the ARM-measured cloud tops. For multi-layered clouds, the radiative centers occur closer to the cloud base of the high-level cloud, or between the higher and lower cloud layers. As a result, the CERES-MODIS H_{eff} PDF and CDF values are close to those derived from ARM radar-lidar observations (Figure 6c). Other seasons, however, tend to feature fewer

upper-level clouds, and low-level clouds become dominant as discussed in Shupe et al. (2011) and demonstrated in Figure 6 in this study. This lowering of physical cloud heights causes H_{eff} to be reported near the cloud physical center from November to June as shown in Figure 5.

The monthly means of H_{base} measured by ARM and CC agree well, remaining between 1 and 2 km throughout the months and averaging within 200 m of each other. Similarly, the monthly means of H_{top} derived from ARM and CC, in general, agree well during the winter and early spring months as demonstrated in Figure 5. The similarities, however, start to deviate after April, when CC H_{top} continues to increase, while ARM H_{top} levels off or slightly decreases, with a maximum difference between CC (7.3 km) and ARM (3.3 km) in September.

Figure 6b clearly illustrates that, during March, the ARM and CC PDFs and CDFs are nearly identical, resulting in similar monthly means of cloud-top heights (Figure 5). During August-September, however, both the PDFs and CDFs differ significantly and can be briefly summarized as follows. Although both ARM and CC CDFs peak at 1 km, their CDFs show that the ARM radar-lidar observed approximately 40% of total clouds, while CC only measured 8% below 1 km. The cloud-top height is about 6 km when the CC CDF is equal to 40%, indicating that CC detected more high-level clouds than ARM. This argument is further proven by greater CC occurrences above 8.5 km than ARM, and more clouds observed by CC above 11 km. As shown in Figure 6c, the ARM CDF reported that 99% of clouds had been measured at a height of 11 km, as opposed to the 84% measured by CC at the same height. The clouds above 8.5 km observed by CC but missed by ARM (and CERES-MODIS) are optically thin cirrus clouds, which remain

undetected by the ARM MPL because of attenuation by low- and mid-level clouds, and are beyond the low detection limit of the ARM MMCR. The optically thin clouds above 8.5 km are entirely observed by CALIPSO, which has been shown by the PDF/CDF and monthly mean cloud-top height comparisons between CloudSat and ARM MMCR, where mean values are nearly the same during September (not shown). Therefore, the large H_{top} difference between CC and ARM throughout the warm months in Figure 5 is due, in large part, to CC limitations in detecting clouds below 1 km and ARM radar-lidar limitations in measuring optically thin upper-level clouds, especially during the summer months when multi-layered clouds are present. This effect of a thin cirrus layer occurring frequently helps explain why the CERES-MODIS cloud-top heights peak around 2 km instead of 1 km, since the thin, high layer would result in an overestimate of the heights for the low clouds retrieved by the algorithm.

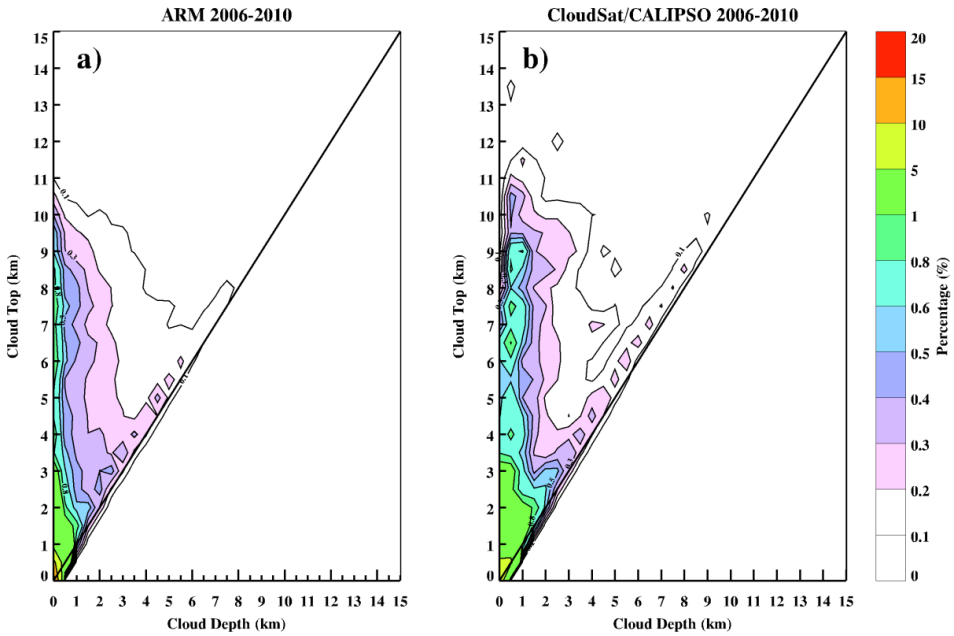

Figure 7. Histograms of cloud-top height vs. cloud depth during the 2006-2010 period for (a) ARM and (b) CC radar-lidar observations. The histograms are normalized by the number of cloudy counts in each 0.5×0.5 km bin to the total number of cloudy counts. Note that contours below the 1:1 line are due to the contouring algorithm used by the plotting program.

To further investigate the cloud-top difference between ARM and CC, the histograms of cloud-top height vs. cloud depth derived from both ARM and CC during the 2006-2010 period are plotted in Figure 7. The histograms first show that more deep clouds, which are identified where cloud-top heights equal cloud depth along the 1:1 line, are observed by CC than ARM. In addition, the percentages of CC-detected highest cloud-top heights are higher than ARM at any given height above 1 km. Finally, the cloud depth (or thickness) observed by CC is greater than that from the ARM observations at a given cloud-top height.

PART 2: Comparison of Cloud Macrophysical Properties over the Arctic

Cloud fractions and cloud heights derived from CERES-MODIS have been compared to those measured by CloudSat/CALIPSO over the span of the Arctic. Data are averaged into grid boxes of 3º latitude × 3º longitude, and cover all longitudes from 61.5ºN to 82.5ºN.

Cloud Fraction

Arctic-wide annual CFs from CC are plotted in Figure 8a, with differences between CERES-MODIS and CC shown in Figure 8b. Differences are calculated using

$$Difference = CF_{MODIS} - CF_{CC} \quad (3)$$

where CF_{MODIS} represents CERES-MODIS cloud fraction and CF_{CC} is cloud fraction determined by CloudSat and CALIPSO.

As Figure 8a illustrates, annual cloud fractions across the Arctic reach a peak in the Greenland and Barents Seas where CC reports the 4-year averaged CF as high as 91.7%. While these averages remain between 60% and 80% across much of the rest of

the Arctic, including the Beaufort Sea, Russia, Siberia, and Canada, a minimum of 53.4% is evident across Northern and Central Greenland.

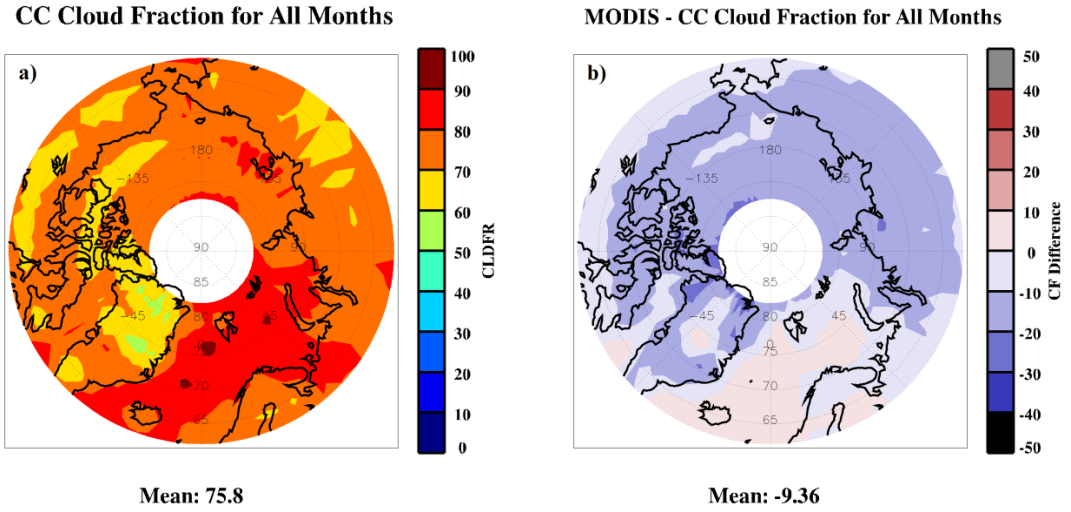

Figure 8. Arctic-wide (a) cloud fractions from CloudSat/CALIPSO and (b) differences in CERES-MODIS and CloudSat/CALIPSO derived cloud fractions for the 2006-2010 period.

The average differences plotted in Figure 8b show that CFs derived from CERES-MODIS agree well with CC through central Greenland, the Greenland and Barents Seas, and into the Scandinavian Peninsula, deviating by no more than ±10% in these regions. Across the majority of the Arctic, however, CFs from CERES-MODIS show underestimates of, on average, between 20% and 30%, with the largest differences of 31% occurring in Northeastern Greenland and the Arctic Ocean, near the Beaufort Sea.

Figures 9 and 10 break Arctic CFs into monthly averages for Northern Hemisphere summer (June, July, and August; JJA) and winter (December, January, and February; DJF) months, respectively. Cloud fractions derived from CC are shown in the top panel, while the differences between CERES-MODIS and CC are presented in the bottom panel.

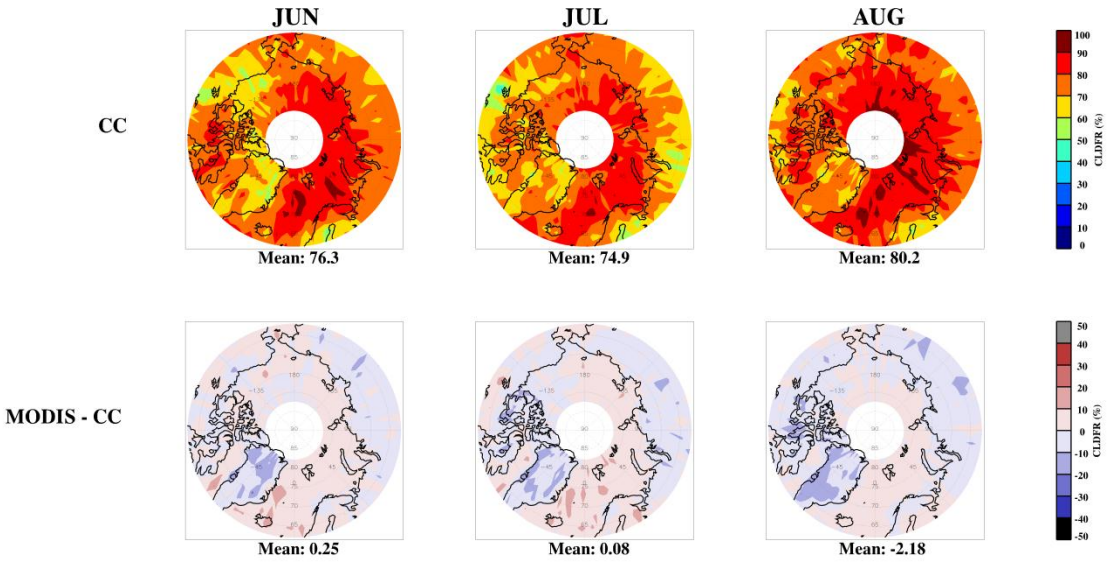

Figure 9. Arctic-wide averaged cloud fractions derived from CC (upper panel) and their differences with CERES-MODIS (lower panel) for JJA.

During the Northern Hemisphere summer, Arctic-wide CFs average to approximately 77.1%, with a range of monthly means from 74.9% in July to 80.2% in August as illustrated in Figure 9. These results are consistent with Kay and Gettelman (2009), who reported a CloudSat/CALIPSO JJA average CF of 77% for the region extending from 65-82ºN. As demonstrated in Figure 9, the averaged CF patterns derived from CC do not vary significantly during the 3-month period. Measurements from CC show the highest cloud fractions occurring over the Greenland and Barents Seas, where CFs are as high as 97.2% in August. Over the Arctic Ocean and into the seas bordering Siberia and Russia, CFs remain nearly constant, averaging between 80% and 90%. Across land areas, CFs are slightly lower, and average to 70-80% in Siberia and Russia, while Greenland and regions of northern Canada experience cloud amounts as low as 43.7% in July.

In general, differences between the active and passive satellite summertime retrievals, shown in the lower panel of Figure 9, remain small, averaging between ±10%

throughout the majority of the Arctic. Deficits in CERES-MODIS CF increase over Greenland, where retrievals dip 20-25% lower than CC through JJA. These underestimates are coupled with overestimates in CERES-MODIS retrieved CFs over the Greenland Sea during June and July, where values exceed those from CC by 21.3% and 16.4%, respectively.

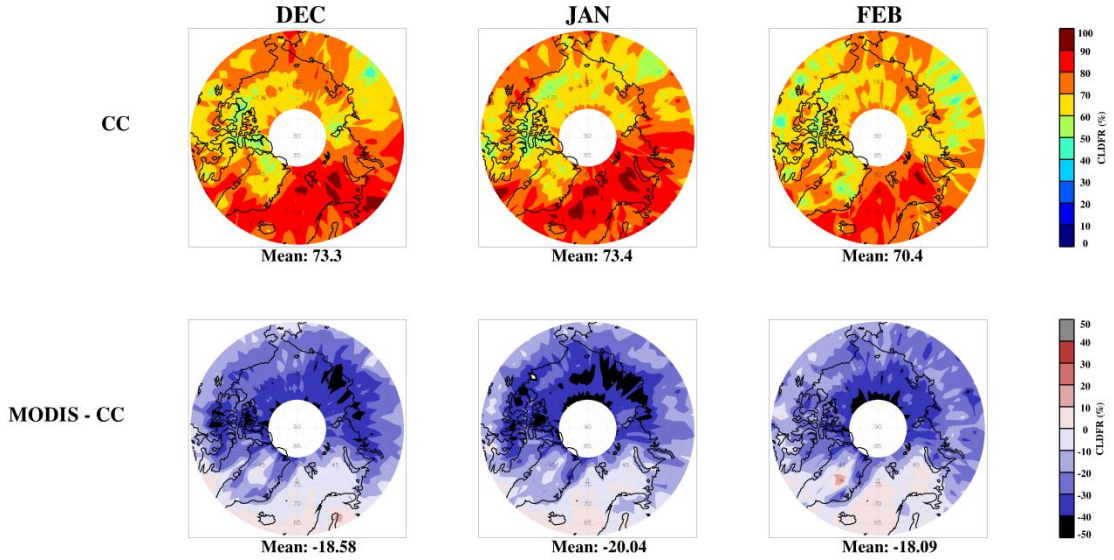

Figure 10. Same as Figure 9, but for DJF.

During DJF, the monthly means of CF derived from CC across the Arctic are slightly lower than those reported during summer months. While Arctic-wide summer averages reach 77.1%, CFs decrease in some regions during the winter, leading to a DJF average CF of 72.4% (Figure 10). These differences mainly stem from a decrease in CF across the Arctic Ocean and its surrounding seas, where, in general, values range from 50-70%, with some higher amounts included. When compared to CC, CERES-MODIS significantly underestimates cloud fractions in these regions, with monthly deviations of -48.7%, -59.2%, and -50.4% in December, January, and February, respectively, as shown in the lower panels of Figure 10. Despite these differences, however, similarities in CF

are seen in DJF and JJA across the Greenland and Barents Seas, where differences between CERES-MODIS and CC fall between ±10%.

Cloud Heights

The 4-year averages of highest cloud-top heights measured by CC, which are displayed in Figure 11a, follow a distinct pattern across the Arctic latitudes. Closest to the North Pole, extending into the Laptev and East Siberian Seas and across the Queen Elizabeth Islands north of Canada, H_{top} is at its lowest, with heights averaging as low as 5.8 km. As latitudes decrease away from the North Pole, H_{top} increases, averaging between 7 and 8 km across Siberia and parts of Russia, and reaching as high as 10.1 km in Iceland.

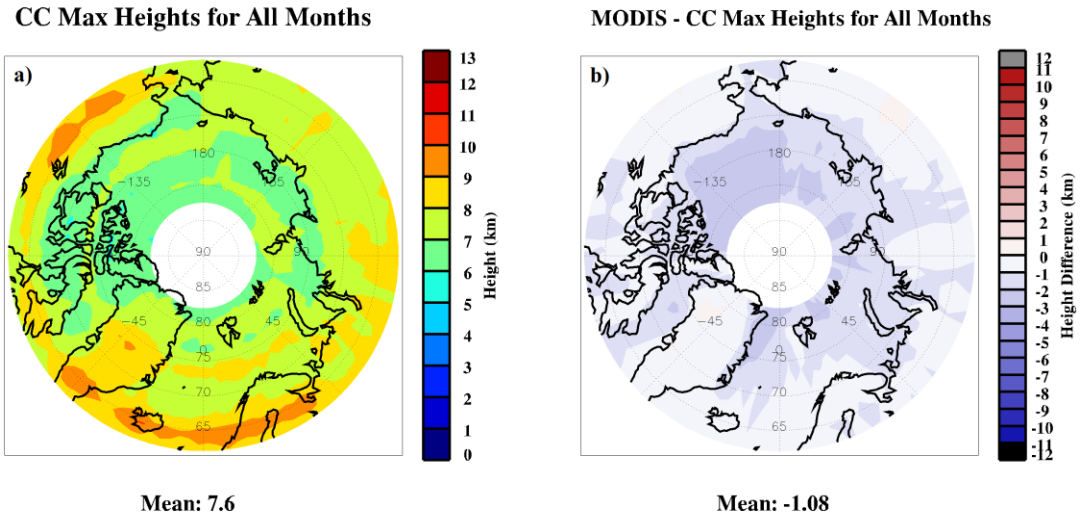

Figure 11. Same as Figure 8, but for cloud heights.

Arctic-wide effective cloud heights from CERES-MODIS over the 4-year period behave similarly to those investigated at the ARM NSA site, as shown in Figure 11b. Differences between CERES-MODIS and CC (Figure 11b) show that CERES-MODIS derived H_{eff} are 0-4 km lower than the H_{top} derived from CC at any given Arctic grid point, with differences increasing toward the North Pole. Over land areas, the cloud

heights derived from CERES-MODIS and CC agree within 1 km. The effective cloud heights over oceanic regions, however, are reported as much as 4.6 km lower than the H_{top} derived from CC.

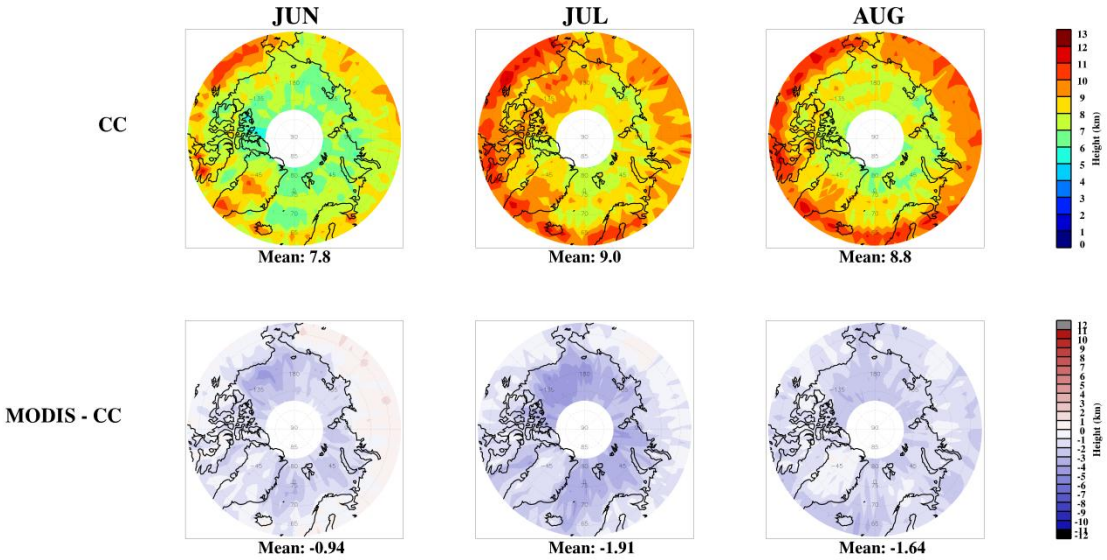

Figure 12. Arctic-wide highest cloud-top heights derived from CC (upper panel) and their differences with CERES-MODIS effective cloud heights (lower panel) for JJA.

During JJA, the CC H_{top} patterns are similar to those shown in annual H_{top} averages (Figure 11a), where the highest clouds occur mainly over the land regions (<65ºN), while the lowest clouds are mostly confined to the oceanic regions. As illustrated in the upper panel of Figure 12, the monthly means of CC H_{top} increase from 7.8 km in June to 9.0 km and 8.8 km in July and August, reaching a peak of 12.2 km in localized regions in August. Averages in the interior Arctic, along the Arctic Ocean and its surrounding seas, however, increase from June into July, where heights raise from around 6 km to 7-8 km, before decreasing again in August to between 6 and 7 km in the northern regions of the Barents and Greenland seas.

Patterns in differences between CERES-MODIS H_{eff} and CC H_{top} during JJA are also similar to the 4-year average differences in Figure 11b. In general, differences in

satellite-derived cloud heights over land areas, including Siberia, Russia, Greenland, and Canada, are small, as displayed in the lower panels of Figure 12. Over these areas, CERES-MODIS H_{eff} fall 0-1 km below CC H_{top} in June and July. One exception is witnessed over Siberia in June, however, where CERES-MODIS overestimates cloud heights by as much as 1.5 km. The largest differences between CERES-MODIS and CC in June and July occur over oceanic regions, where CC detects clouds as much as 5.2 km higher than CERES-MODIS. During August, however, these dissimilarities decrease slightly, with CERES-MODIS derived H_{eff} falling, on average, 3-4 km below the CC-measured H_{top}. Conversely, over land areas, differences in satellite retrievals increase slightly to 1-2 km.

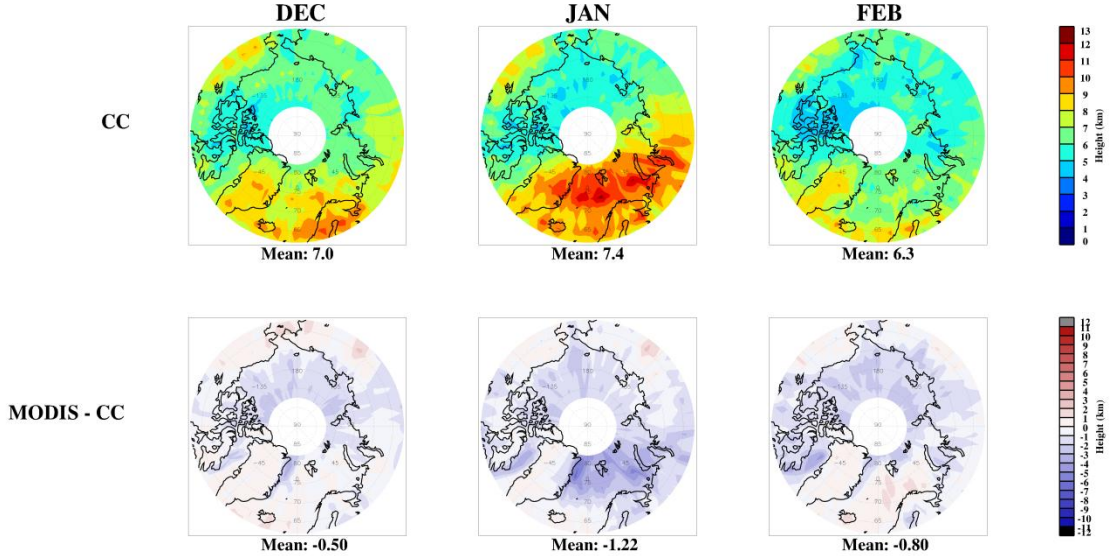

Figure 13. Same as Figure 12, but for DJF.

While clouds measured by CC during the Northern Hemisphere summer follow patterns similar to those displayed in Figure 11a, measurements during DJF, shown in the upper panel of Figure 13, differ significantly. In JJA, the H_{top} weighted average is 8.5 km (Figure 12), but cloud heights over many regions, including the Arctic Ocean, Beaufort

Sea, Siberia, and Canada, decrease during the winter, resulting in an averaged H_{top} of 6.9 km. The highest CC cloud altitudes occur over the Barents and Greenland Seas during winter, where regional averages reach 7.5, 9.9, and 6.6 km in December, January, and February, respectively. Alternatively, over the Beaufort, East Siberian, and Laptev Seas, cloud heights are much lower with an average value of ~6 km.

During the winter months (DJF), the CERES-MODIS H_{eff} values agree relatively well with CC H_{top}, particularly over land areas, where differences lie mainly within ±1 km, as demonstrated in the lower panels of Figure 13. The largest differences in December and February occur across the Beaufort, East Siberian, and Laptev Seas, where the lowest Arctic cloud heights occur, while January shows CERES-MODIS H_{eff} underestimates across the Barents and Greenland Seas.

Discussion

Cloud macrophysical properties retrieved from CERES-MODIS face unique struggles during winter months when direct solar radiation is not available. During this time, sea ice is prevalent across most Arctic waterways, as Figure 14 from the National Snow and Ice Data Center (NSIDC) shows. This image documents the extent of sea ice concentration in January of 2007 and shows a distinct line bordering Greenland and the Barents Sea where the edge of sea ice meets open water. This region tends to remain free of sea ice year-round, mainly because of the influx of warm currents from the Atlantic Ocean (Arthun et al. 2012).

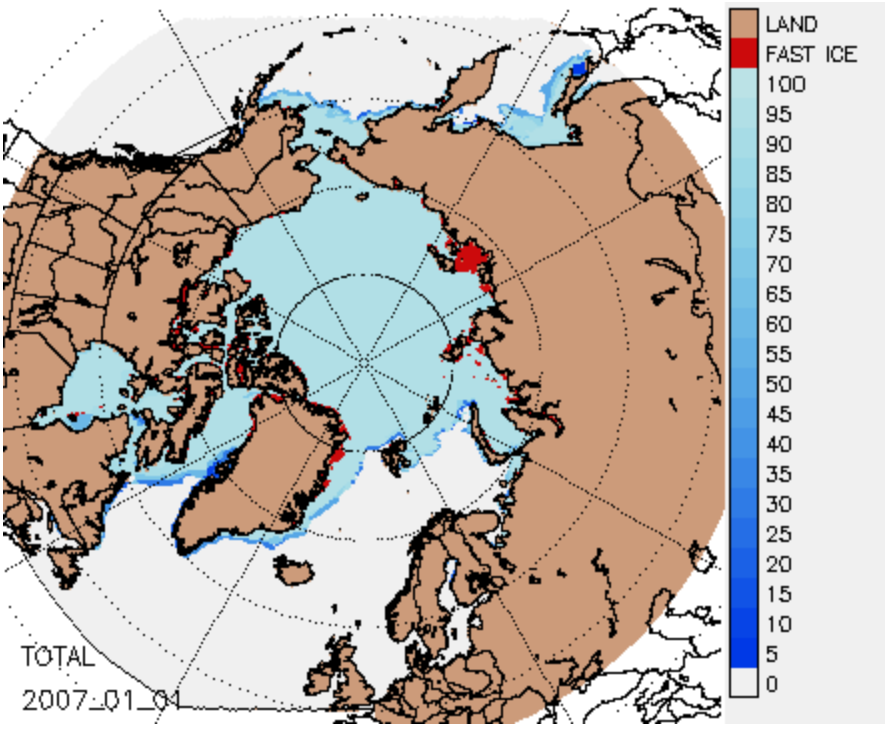

Figure 14. Image of sea ice extent for the week of January 1, 2007, from the National Snow and Ice Data Center.

Differences between CERES-MODIS and CC cloud fractions during DJF capture the regions of sea ice and open water well. In the lower panels of Figure 10, a distinct line nearly identical to the edges of the sea ice extent shown in Figure 14 separates the Greenland and Barents Seas from the rest of the Arctic. Across these two bodies of water, cloud fractions between CC and CERES-MODIS are similar. However, throughout the rest of the Arctic, CERES-MODIS severely underestimates CF. Similar results were found by Liu et al. (2010), who used data from July 2006 to December 2008 and concluded that MODIS CFs during polar night decrease with increasing sea ice concentration compared to CloudSat and CALIPSO results. This indicates that SINT algorithms used in retrieving CERES-MODIS cloud properties over snow and ice surfaces struggle to capture accurate cloud fractions during polar night.

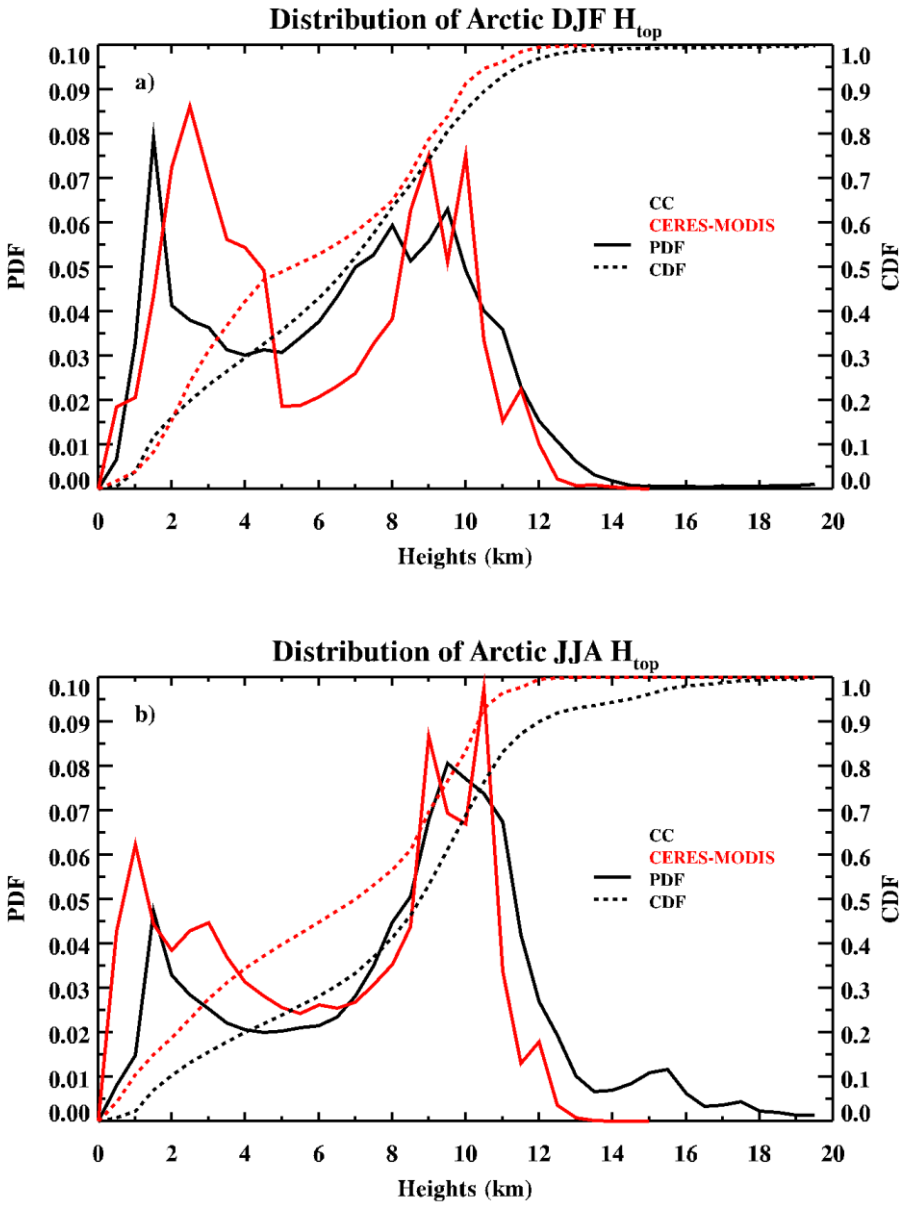

Figure 15. Vertical distribution of CC highest cloud-top heights (black) and CERES-MODIS effective cloud heights (red) across the entire Arctic for (a) DJF, and (b) JJA. Solid lines represent the PDF, while dashed lines represent the CDF.

As discussed above, the CERES-MODIS derived CFs during winter months are much lower than those derived from CC, however, this is not the case for the cloud height comparison. In fact, differences in cloud heights are actually smaller during DJF than during JJA. To further investigate these differences, the PDFs and CDFs of H_{top} and H_{eff} during DJF and JJA are plotted in Figures 15a and 15b, respectively. As demonstrated in

Figure 15a, the cloud heights derived from CC and CERES-MODIS over the Arctic during DJF have a bimodal distribution with a lower peak between 1.5 and 2.5 km and a higher one between 8 and 10 km. In addition to the good agreement in their PDFs, their CDFs also agree well, particularly in the lowest levels and above 9 km. The vertical distributions of H_{top} and H_{eff} during JJA are similar to their winter counterpart with a bimodal distribution. However, CC detected clouds about 2 km higher than those retrieved from CERES-MODIS. At an altitude of 12 km, the CERES-MODIS CDF is 100%, while the CC CDF is only 90%. These clouds (above 12 km) are likely optically thin cirrus clouds that the CERES-MODIS channels have difficulty detecting, due to its limit in detecting clouds with optical depths less than 0.3 (Chiriaco et al. 2007; Minnis et al. 2008).

PART 3: Comparison of Cloud Macrophysical Properties over the Antarctic

Cloud fractions and cloud heights derived from CERES-MODIS have been compared to similar measurements from CloudSat/CALIPSO over the Antarctic. Data are averaged into grid boxes of 3º latitude × 3º longitude, and cover all longitudes from 61.5ºS to 82.5ºS.

Cloud Fraction

Across the Antarctic, distinct differences in cloud fraction are seen over land and ocean areas. Unlike the Arctic, which is characterized by a large body of water and ice surrounded by land (Figure 2), Figure 16 shows that the Antarctic is composed of a large land mass surrounded by water, known as the Southern Hemisphere storm track. Over

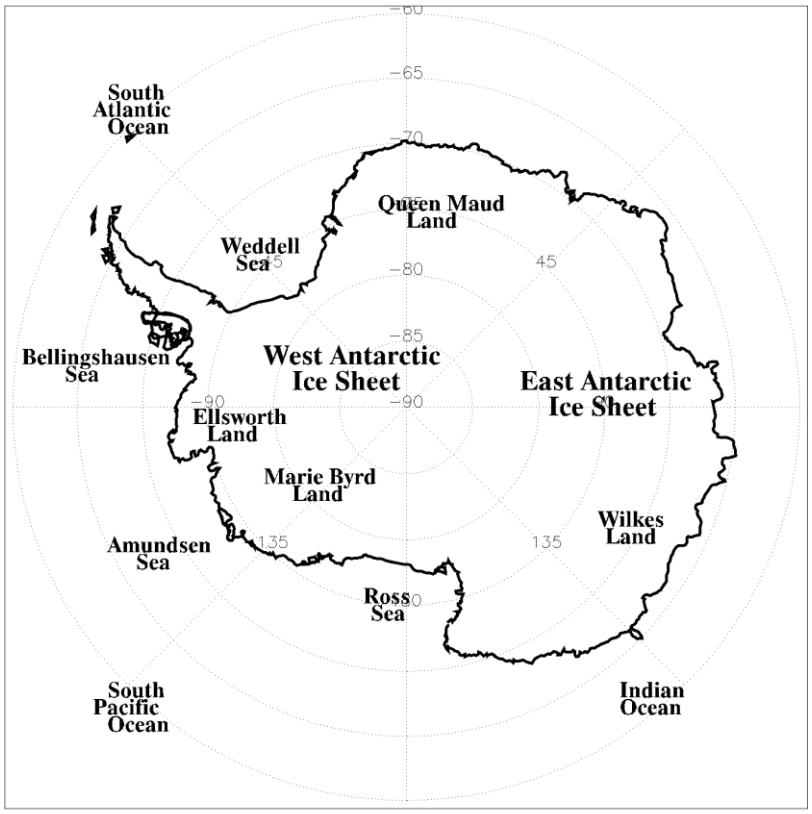

Figure 16. Reference map of Antarctic locations.

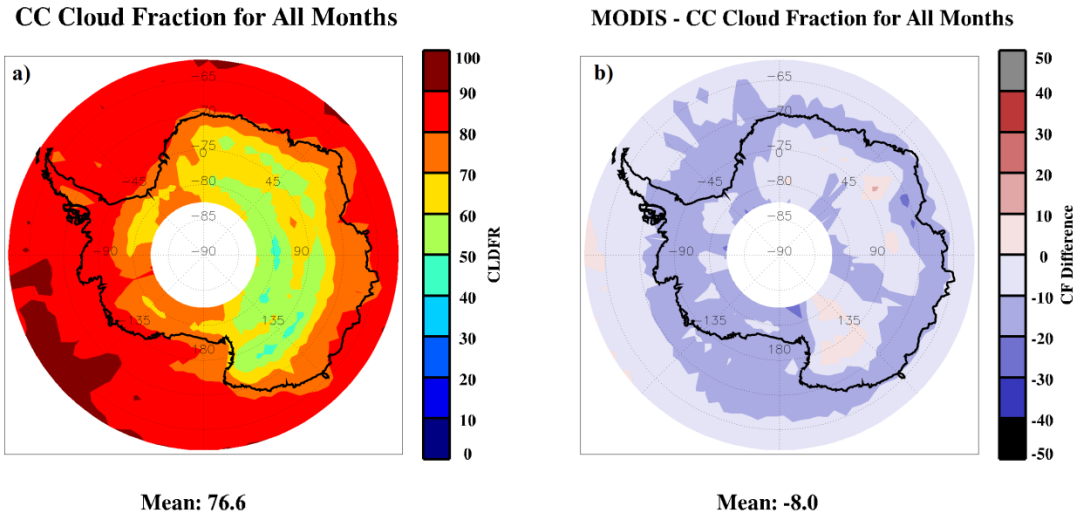

Figure 17. Antarctic-wide (a) cloud fractions derived from CC radar-lidar measurements and (b) CERES-MODIS and CC differences during the period 2006-2010.

land, especially in the interior regions of the continent east of the Transantarctic Mountains, which run along a line from the coast of the Ross Sea up to the Weddell Sea, cloud fractions are small. As shown in Figure 17a, the mean CFs average as low as 43.6% across this region during the 4-year period. Around the land-ocean border of Antarctica, however, cloud fractions range between 70 and 80%, increasing to as much as 80-90% over the Antarctic Peninsula between the Weddell and Bellingshausen Seas and across most of the oceanic area surrounding the continent.

Compared to CC-detected CFs, CERES-MODIS CFs across the ocean and over the East Antarctic Ice Sheet are nearly the same, with agreements within ±10% in the 4-year averages (Figure 17b). Around the border of Antarctica, into the Ross Sea, and across the Weddell Sea, the CF differences between CC and CERES-MODIS increase to 10-20%, with a peak difference of -29.5% occurring over the land south of the Ross Sea.

During December-February, the Southern Hemisphere summer months, cloud fractions over the waters surrounding Antarctica are much higher than their annual averages (Figure 17a). This is evident in Figure 18, where the CFs derived from CC reach peaks between 96% and 98% during each of the 3 months. Across the East Antarctic Ice Sheet, CC cloud fractions remain low through the duration of the season, averaging to 50.3%, 55.0%, and 50.0% in December, January, and February, respectively. This coupling of high and low CFs leads to a seasonal average of 76.1%. These results are consistent with those from both Bromwich et al. (2012) and Adhikari et al. (2012), who investigated CFs from CloudSat and CALIPSO during similar 4-year periods.

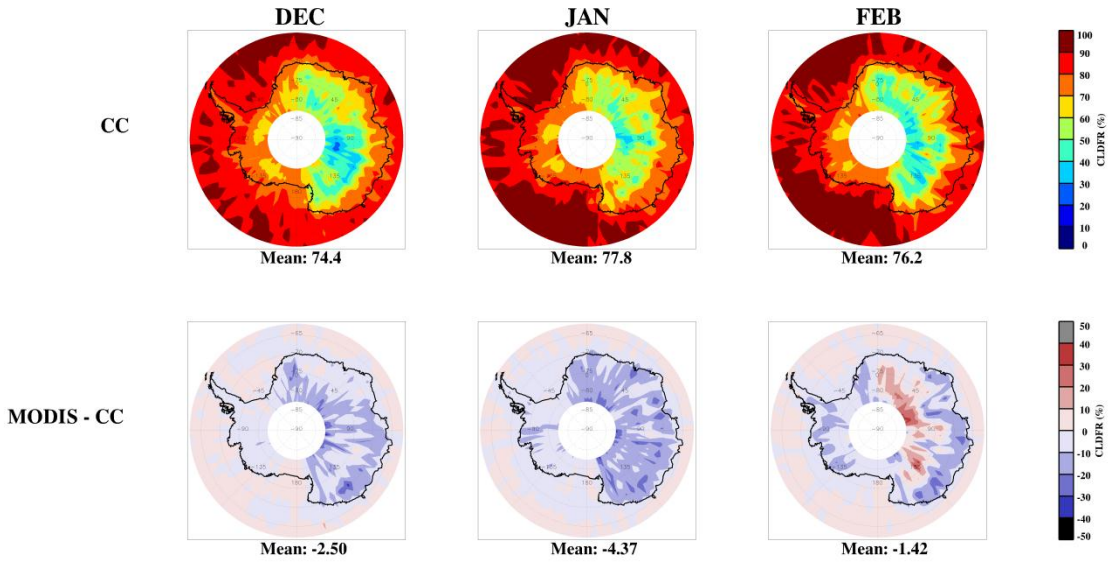

Figure 18. Antarctic-wide CC detected CFs (upper panels) and differences with CERES-MODIS (lower panels) for DJF.

CERES-MODIS captures CFs over the ocean, Antarctic Peninsula, and most of Marie Byrd Land well. The lower panels of Figure 18 show that CERES-MODIS CFs range no more than 10% higher or lower than CC in these regions. Cloud fractions over the East Antarctic Ice Sheet present more of an issue, however. During December, differences between CERES-MODIS and CC CFs are, in general, small, though localized regions across Wilkes Land and in the East Antarctic Ice Sheet closer to the South Pole experience CERES-MODIS CF deficits of as much as 38.2%. During January, CERES-MODIS underestimates of 20-30% spread across the majority of the East Antarctic Ice Sheet. In February, however, CERES-MODIS detects, in general, between 10 and 30% more clouds than CC over the same location, with overestimates of up to 46% reported nearest to the South Pole at a longitude of ~70ºE.

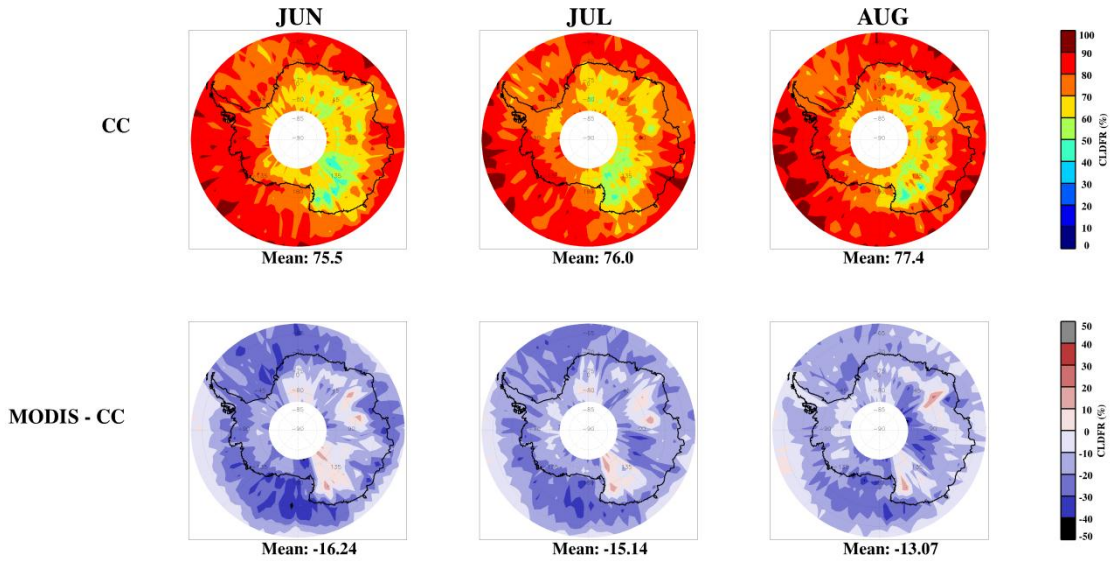

Figure 19. Same as Figure 18, but for JJA.

Cloud fraction patterns derived from CC during the Southern Hemisphere winter months, June-August, are very similar to their DJF counterparts as illustrated in Figure 18. As shown in Figure 19, CC CFs are, once again, highest over the ocean, with decreasing cloud amounts over the interior part of the continent. During JJA, however, cloud fractions across the Southern Hemisphere storm track are noticeably lower than those in the same region during DJF, remaining, in general, between 70 and 90%, except in August when CFs jump a bit higher near the Amundsen and Bellingshausen Seas. High CFs are also prevalent along Wilkes Land and Ellsworth Land in coastal Antarctica, where values exceeding 70% persist during July and August. A lower average of 64.4% is found over the extent of the East Antarctic Ice Sheet, with values as low as 35% reported to the east of the Transantarctic Mountains in both June and August.

The bottom panels of Figure 19 show that CERES-MODIS algorithms underestimate CF by a large percentage across many parts of the Antarctic during JJA. Through the duration of the Southern Hemisphere winter months, CERES-MODIS CFs

reported across the Southern Hemisphere storm track, west of the Transantarctic Mountains, and into Wilkes Land fall 20-30% lower than the CFs (80-90%) derived from CC. The largest differences occur in June, however, when CERES-MODIS CFs are around 43% lower than those derived from CC in the Ross Sea. The CERES-MODIS derived CFs overestimate values by 10-20% than CC results over regions east of the Transantarctic Mountains and across portions of the East Antarctic Ice Sheet, as demonstrated in the lower panels of Figure 19.

Cloud Heights

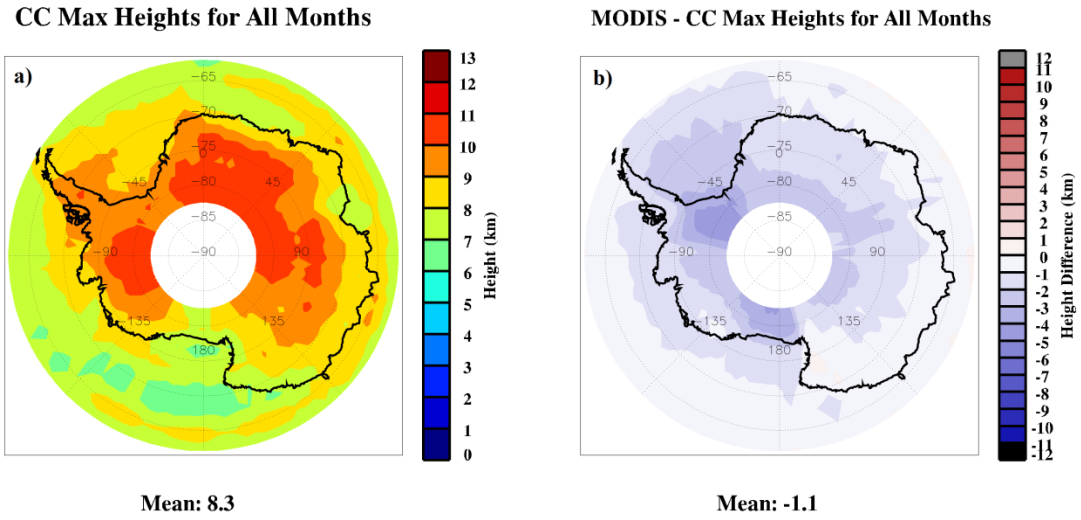

Figure 20. Same as Figure 17, but for cloud heights.

Figure 20a shows the 4-year averages of CC-measured highest cloud-top heights over the entire Antarctic where more high-level clouds occur over land, whereas more low-level or mid-level clouds occur over the surrounding oceans. Cloud heights in the central portion of the continent, extending across Ellsworth Land, Queen Maud Land, and the interior portion of the East Antarctic Ice Sheet, range between 10 and 11 km and

represent the highest averages during the 4-year period. Along the Antarctica coast, including Wilkes Land and the outer reaches of Marie Byrd Land, cloud heights drop to 8-9 km, and decrease further into the Southern Hemisphere storm track, where H_{top} ranges between 6 and 9 km.

Effective cloud heights retrieved from CERES-MODIS agree with CC results in most of the surrounding water areas well, falling no more than 1 km lower than CC in all regions except the Weddell Sea and near the land bordering the Bellingshausen, Amundsen, and Ross Seas. As illustrated in Figure 20b, these 1-km discrepancies continue across Wilkes Land and into coastal portions of the East Antarctic Ice Sheet. Differences in measured CC H_{top} and CERES-MODIS derived H_{eff} increase as latitudes progress towards the South Pole. These differences are maximized in the two locations closest to the Weddell and Ross Seas, where CERES-MODIS H_{eff} values fall between 4 and 5 km lower than CC.

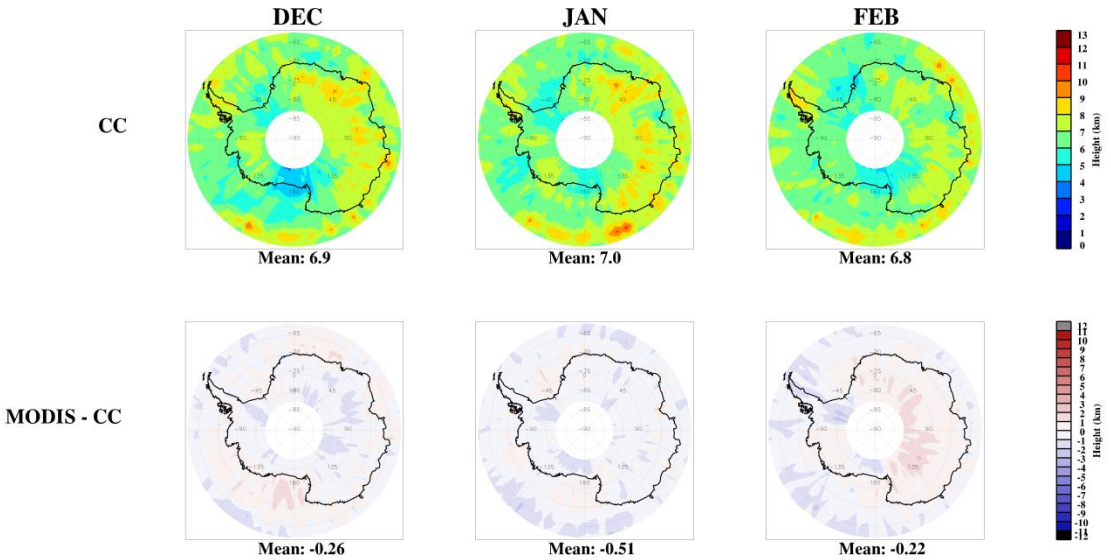

Figure 21. Antarctic-wide CC highest cloud-top heights (upper panels) and their differences with CERES-MODIS effective cloud heights (lower panels).

During DJF, the cloud heights measured by CC are much lower than the annual mean, with an average of 6.9 km and similar monthly means during the 3 months (Figure 21). The lower cloud-top heights occur over the land bordering the Ross Sea, where averages of CC H_{top} do not exceed 6 km throughout the duration of the season. A string of higher H_{top}, with altitudes of 7-10 km, connects the South Pacific and Indian Oceans. Similar cloud heights stretch across the East Antarctic Ice sheet through the duration of the summer.

Presented in the lower panels of Figure 21 for DJF, the effective cloud heights retrieved from CERES-MODIS agree with CC H_{top} within ±1 km throughout a large portion of the Antarctic. Regions of slightly larger underestimates in H_{eff} occur along a band connecting the South Pacific and Indian Oceans, over the land near the Ross Sea, and over a small portion of the West Antarctic Ice Sheet near the Weddell Sea through the duration of the season. Among these locations, H_{eff} values from CERES-MODIS fall roughly 2-3 km lower than H_{top} values from CC. The maximum underestimate of H_{eff} throughout the season occurs over the land near the Weddell Sea in February, where CERES-MODIS H_{eff} retrievals fall ~2.9 km below CC. The largest overestimates of CERES-MODIS H_{eff} are also seen in February, when CERES-MODIS retrievals exceed CC H_{top} measurements over a majority of the East Antarctic Ice Sheet. These overestimates reach as high as 2.4 km above CC, though most of the overestimates range 1-2 km higher.

During JJA, cloud heights derived from CC (Figure 22) are much higher than their annual mean and DJF averages over most of the Antarctic regions, particularly over land. In June, H_{top} values are greater than 12 km across the Weddell Sea and most of the

Antarctic land mass, with maximum values reaching 18.4 km into the atmosphere. This region of high H_{top} remains a constant feature through the JJA months, with the July maximum reaching 19.0 km, and August experiencing a slightly decreased maximum H_{top} of 17.7 km. The lowest cloud heights reported throughout the season occur over Wilkes Land and the oceans surrounding Antarctica, where H_{top} falls between 5 and 8 km.

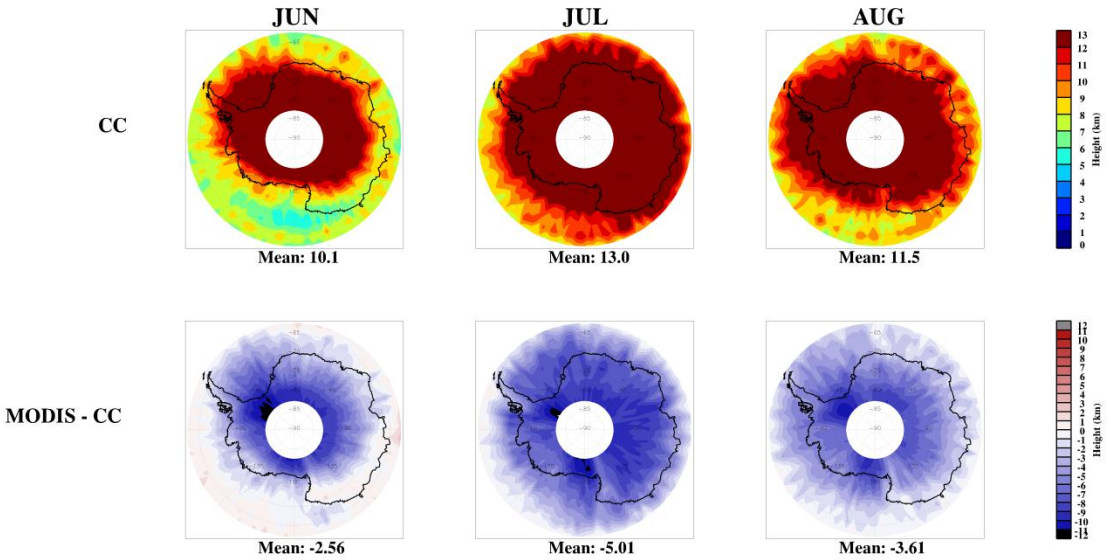

Figure 22. Same as Figure 21, but for JJA.

While CERES-MODIS is able to detect the lower cloud heights over Wilkes Land, the South Pacific Ocean, and the Indian Ocean, it is clear from the lower panels of Figure 22 that the algorithms are unable to detect the high clouds that CC measured across the remaining portions of the Antarctic. The pattern of large differences closely resembles the patterns of highest cloud heights in the upper panels. Within these regions, the differences between H_{eff} and H_{top} have a large range from 1 km to 12.3 km in July.

Discussion

Across the Antarctic, cloud fractions and heights derived from the satellites exhibit similar features as discussed for the Arctic. In general, CERES-MODIS and CC both report similar cloud heights and cloud fractions during DJF, while JJA are characterized by large underestimates in CERES-MODIS retrievals of cloud macrophysical properties. One clear difference, however, is the presence of large CERES-MODIS overestimates in CF during February over Antarctica. Similar findings were reported by Minnis et al. (2007), who compared global mean CF from CERES-MODIS, CALIPSO, and CloudSat for April of 2007. In this study, it was found that CALIPSO cloud fractions exceeded those from both CloudSat and CERES-MODIS in most regions. Over the Antarctic, however, CERES-MODIS results were substantially higher, due to the instrument detecting too many extremely cold clouds. The reasons for this phenomenon are still under investigation.

During DJF, Arctic CFs derived from CERES-MODIS were much lower than CC results, resulting from little to no direct solar radiation and small thermal contrast between clouds and snow-ice covered surfaces. While this effect undoubtedly causes similar issues in the Antarctic during JJA, it does not explain the extreme differences witnessed in retrievals of cloud heights that were not present in ARM NSA or Arctic comparisons.

To further investigate these discrepancies, the PDF and CDF for Antarctic-wide H_{top} and H_{eff} during JJA were plotted using 500 m height bins. As demonstrated in Figure 23, both the PDF and the CDF from CC and CERES-MODIS are nearly the same below 8 km, and start to deviate above 8 km. Both platforms show that cloud heights

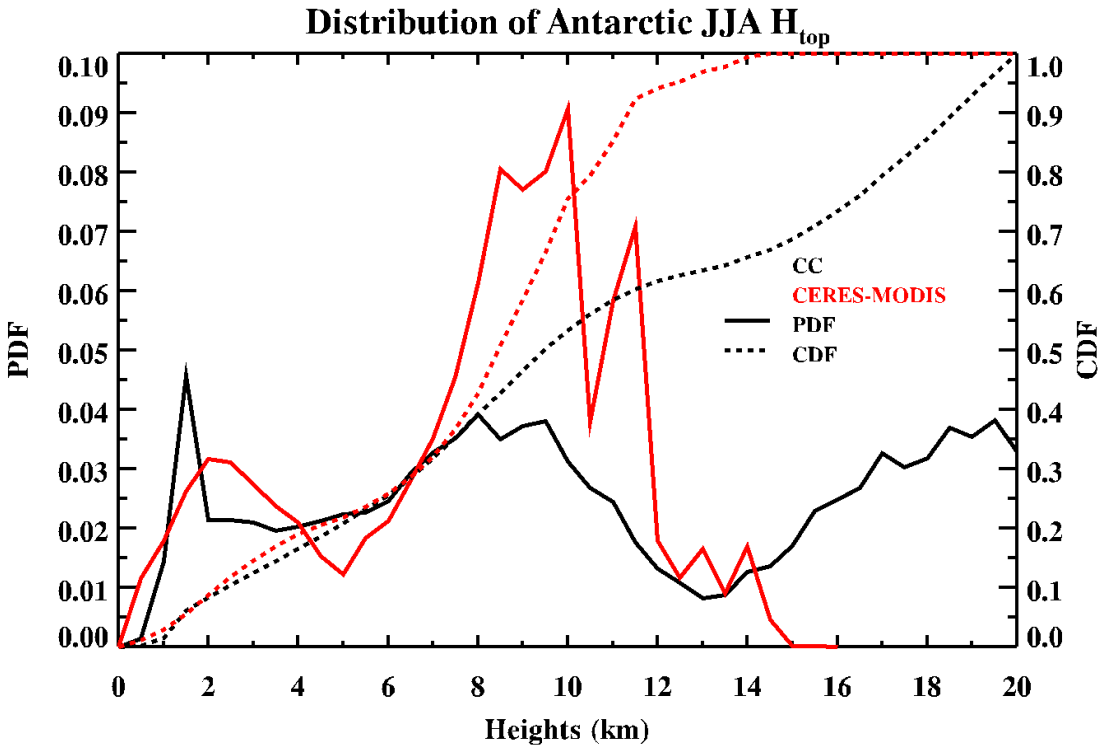

Figure 23. Vertical distribution of CC highest cloud-top heights (black) and CERES-MODIS effective cloud heights (red) across the Antarctic for JJA. Solid lines denote the PDF, while dashed lines represent the CDF.

exhibit an initial peak near 2 km, and CDFs show that CERES-MODIS and CC have both observed approximately 40% of total clouds by a height of 8 km. After this level, CERES-MODIS shows an overall peak in clouds at 10 km, with the CDF reporting that 99% of CERES-MODIS clouds were detected within the lowest 14 km of the atmosphere. At this same altitude, however, CC has only detected 66% of its total clouds. The CC distributions, overall, are more spread out, with relative PDF maximums of 0.04 occurring at 8 and 19.5 km. It is not until a height of nearly 20 km that 99% of CC clouds have been detected. This percentage of clouds detected by CC at high altitudes, coupled with higher CC cloud fractions during the JJA season suggests that CC

is detecting polar stratospheric clouds that are beyond the detection limits of the CERES-MODIS instruments.

Many studies (e.g. Wang et al. 2008; Pitts et al. 2007; Noel and Pitts 2012) have stated that the occurrence of PSCs drops significantly after mid-late September, when solar radiation returns to Antarctica and stratospheric ozone loss begins. This is reflected by Verlinden et al. (2011), who investigated the vertical profiles of cloud occurrence over several regions across the Antarctic using combined CloudSat and CALIPSO data. From this study, it was shown that, across the Antarctic Peninsula, West Antarctica, and the Antarctic Plateau, which extends across the East Antarctic Ice Sheet, clouds occur as high as 25 km during JJA, indicating the presence of PSCs. During September, October, and November, however, the occurrences of clouds above 20 km decreases to nearly 0, indicating that both the height and frequency of PSCs decreases after the winter months. This is indicated further during DJF, where no clouds were reported above ~11 km, regardless of location. Similar patterns of high clouds during winter are not present in the Arctic cloud heights shown in Figure 13. While PSCs have been studied in the Arctic (e.g. Santee et al. 2002; Cheremisin et al. 2007), the Arctic stratosphere is rarely cold enough and lacks the chemical transport required to support PSC formation (Santee et al. 2002; Waibel et al. 1999).

PART 4: Comparison of Single-Layered Low-Level Cloud Microphysical Properties at ARM NSA Site

Time series plots for all daytime, single-layered stratus cases, without and with snow and ice covered surfaces are shown in Figures 25-27, respectively. Figure 24 shows all available instances when daytime low-level stratus clouds occurred between July 2006 and December 2007 for both Terra (Figure 24a, c, and e) and Aqua (Figure

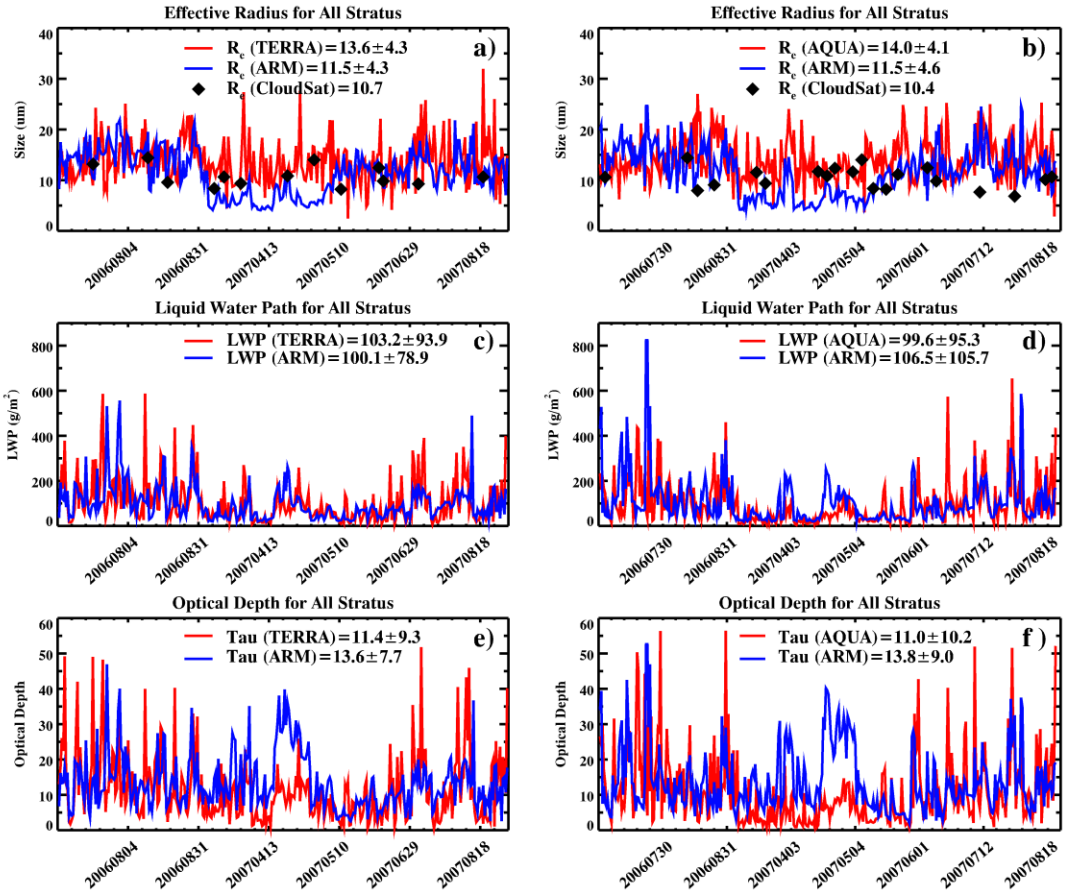

Figure 24. Time series of ARM retrieved cloud-droplet effective radius (a and b), liquid water path (c and d), and optical depth (e and f) with matched MODIS Terra (a, c, and e) and Aqua (b, d, and f) and CloudSat radar-only retrievals for daytime single-layered stratus clouds from July 2006 through December 2007. The cases are ordered from July 2006 to December 2007 for both Terra and Aqua, and exclude dates during polar night when SZA < 82º.

24b, d, and f). The CERES-MODIS retrieved r_e values for both Terra and Aqua are nearly identical and agree well with the ARM results, showing a deviation of about 2.6 μm above the ARM means of 11.5±4.2 μm and 11.5±4.5 μm, respectively. Similar disagreements are seen in the τ retrievals, where the Terra averages are 11.7±9.2 compared to the ARM-derived 13.4±7.5, while the Aqua mean drops to 10.3±9.6 in contrast to the 13.5±8.6 reported by ARM. Liquid water paths for CERES-MODIS were

calculated based on the relationship between r_e and τ in Equation 1, and also reflect small disagreements similar to those seen in r_e and τ. Looking at Figure 24 carefully, it is found that there are considerable differences in r_e and τ in Terra from 31 August 2006 to 10 May 2007 (cases 100 through 200) and in Aqua over roughly the same time period (cases 100 through 250). These cases warrant further investigation.

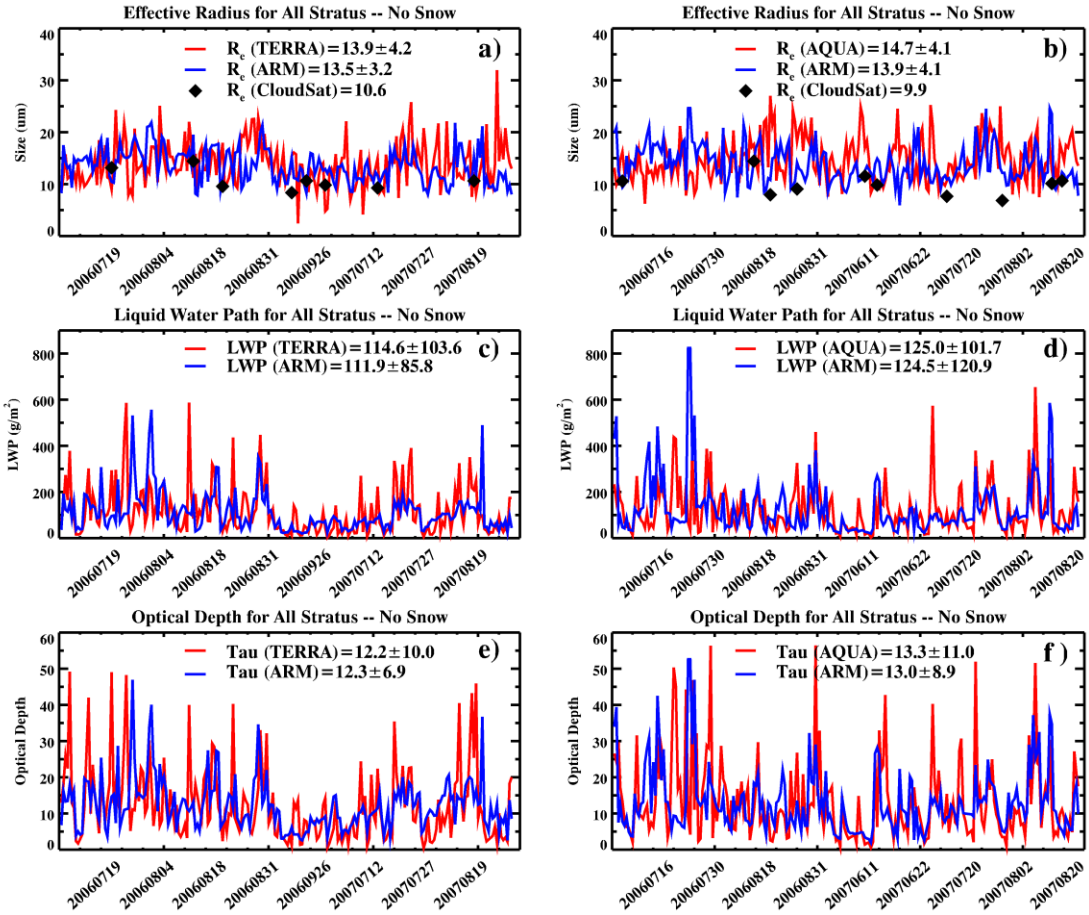

Figure 25. Same as Figure 24, but for cases when land was snow-free.

To investigate the impact of snow and ice on the cloud microphysical retrievals, the stratus cases in Figure 24 have been broken down into those without and with snow and ice covered surfaces, as shown in Figures 25 and 26, respectively. As illustrated in Figure 25, the ARM and CERES-MODIS retrieved r_e values without snow are slightly

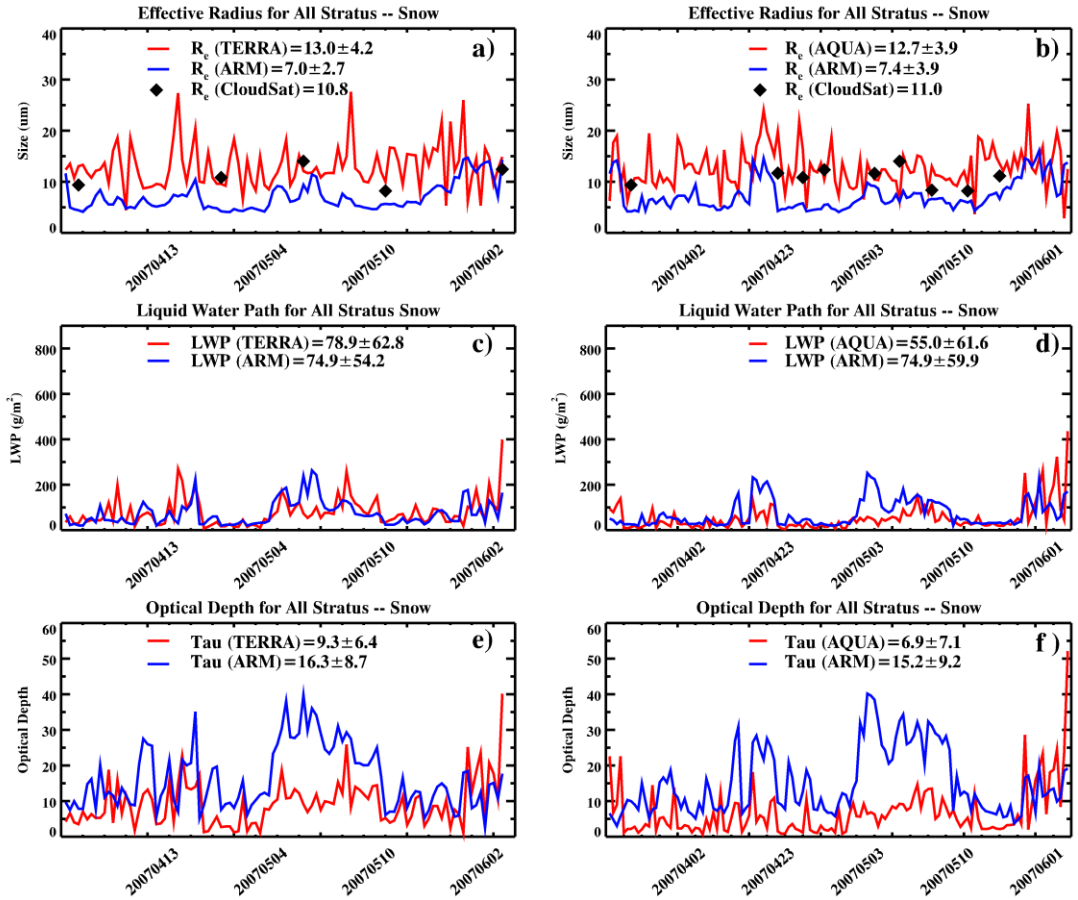

Figure 26. Same as Figure 24, but for cases when land was covered by snow.

larger than those from all stratus cases, and their differences fall with ~1.5 μm. The CERES-MODIS retrieved τ values for Terra improve slightly relative to ARM, but much greater improvements are seen for Aqua when compared to those from all stratus cases. Similar trends also occur for the LWP comparisons. With the presence of snow influencing the background surface, the average r_e differences between ARM and CERES-MODIS for Terra and Aqua, respectively, are ~5.4 and 4.8 μm, values ~3.5 times greater than those without snow (Figure 26). The τ differences between ARM and CERES-MODIS for both Terra and Aqua become larger with the addition of snow at the surface.

Discussion

The ARM surface retrievals in Figures 25 and 26 are nearly the same as those in Dong and Mace (2003). In Table 2 of Dong and Mace (2003), they summarized that the monthly mean r_e values increased from 7.8 μm in May to 13.4 μm in July and fell to 11.5 μm in September, whereas the τ (LWP) values decreased from 17.7 (94.1 gm^{-2}) in May to 8.6 (74.8 gm^{-2}) in July and climbed to 13.8 (107.4 gm^{-2}) in September. Minnis et al. (2011b) noted that the 2.1 μm retrievals of τ for Aqua MODIS data are roughly half those retrieved from Terra MODIS using the 1.6 μm channel, mainly because the wrong atmospheric absorption optical depths were used in the retrievals. However, the large discrepancies between CERES and ARM over snow surfaces cannot be explained by incorrect atmospheric absorption since both satellites produce similar discrepancies.

Table 1. Daytime cloud microphysical property differences (CERES – ARM) and correlation coefficients (R^2), July 2006 – December 2007.

	Terra					**Aqua**				
	No Snow									
	Mean	Mean (%)	SD	SD (%)	R^2	Mean	Mean (%)	SD	SD (%)	R^2
r_e	1.3 μm	9.6	5.2 μm	38	-0.01	1.7 μm	12.3	5.3 μm	38	-0.03
τ	-0.6	-4.9	7.5	61	0.53	-1.2	-9.4	10.2	80	0.41
LWP	1.7 gm^{-2}	1.5	86.6 gm^{-2}	79	0.44	-7.6 gm^{-2}	-6.4	132 gm^{-2}	111	0.21
	Snow									
r_e	5.4 μm	76.0	3.9 μm	55	0.23	4.8 μm	66.7	3.5 μm	49	0.28
τ	-4.4	-27.2	12.6	78	0.15	-7.1	-47.0	10.5	70	0.23
LWP	26.3 gm^{-2}	35	108.4	144	0.26	-8.6 gm^{-2}	-11.8	76.5	105	0.35

Table 1 summarizes the comparisons of the microphysical properties for both snow-covered and snow-free conditions. Despite the good agreement for snow-free

surfaces, the standard deviations (SD) of the differences are quite large for most parameters, reaching as high as 111% for Aqua LWP. Similarly, the SDs over snow-covered surfaces are as great as 144% for Terra LWP. The correlation coefficients, R^2, are relatively low, particularly for r_e. These results contrast with earlier comparisons of CERES-MODIS data with retrievals from data at the ARM Southern Great Plains Central Facility (Dong et al. 2008). There, in snow-free conditions, R^2 was ~0.41, 0.92, and 0.91 for r_e, τ, and LWP, respectively. The corresponding mean standard deviations were ~24, 25, and 35%. Thus, over NSA, the comparison uncertainties increased by a factor of 2-3.

The large discrepancies in SD and R^2 between the NSA and SGP results are likely due to several factors, especially averaging area and surface albedo differences. Dong et al. (2008) used pixel-level results averaged over a 30 km × 30 km area centered on the SGP site. For this study, since pixel-level results were not saved for CERES Ed2 over the NSA, SSF data within the 1° latitude × 3° longitude box centered over the NSA site were averaged. Thus, the averaging box is roughly 111 km × 115 km. Increasing the comparison box size from 30 km to more than 100 km will raise the variability in the differences and make the satellite results less representative of the instant surface observations, but can be representative over the long term. Increasing the averaging area further will eventually disconnect satellite averages from the ground-based means. For example, if a 3°×3° average is used, the mean non-snow Terra and Aqua τ values are only about half of their ARM counterparts, while they are in good agreement for the grid box size used here.

The grid box centered at the Barrow NSA site likely increases the complexity of surface albedo effect on satellite retrievals because the site is located on the coast with

variable sea ice and snow cover. The specification of surface albedo in the retrieval algorithm relies on relatively coarse ice-snow maps that are themselves more uncertain in coastal areas. Conversely, the SGP is in an area having a relatively homogeneous land/vegetation cover with few snow episodes throughout the year. In addition to the potential for albedo effects on the satellite retrievals, the properties of the clouds over water could differ from those over the adjacent land in any given situation. The NSA site will experience one type or the other depending on the winds at the measurement time, while the satellite will measure both. Thus, greater SDs and reduced correlations are expected over the NSA compared to the same parameters over the SGP site for both snow and snow-free scenes.

The averaged r_e values, retrieved from CloudSat radar and matched ARM and MODIS samples, are 10.6 μm, 11.5, and 14.2 μm, respectively, for all stratus cases. Both CloudSat radar and MODIS retrieved r_e values for snow-free (22 samples) and snow–covered (16 samples) surfaces are roughly the same as their respective values for all stratus cases, but the ARM retrievals are 13.7 and 7.2 μm, respectively, for snow-free and snowy surfaces. The radar retrieval is not affected by variations in surface albedo or partially absorbing bands as seen for the CERES-MODIS retrievals, yet no changes are seen in the results when surface conditions change. This lack of variation when snow and ice are present may be due to the inability of the radar to detect the smaller droplets in the clouds present during snowy periods. The retrieval may also be affected by the radar missing lower portions of some of the clouds.

CHAPTER V

CONCLUSIONS

In this study, an evaluation of passive satellite retrievals in polar regions has been conducted. Cloud macrophysical cloud properties derived from active and passive sensors have been compared at the DOE ARM NSA site in Barrow, Alaska, across the extent of the Arctic, and across the Antarctic. At the DOE ARM NSA site, cloud fractions and heights derived from ARM MMCR, MPL, and ceilometer are compared to CC and CERES-MODIS from July 2006 to June 2010. Over the Arctic and Antarctic, CC and CERES-MODIS cloud fractions and heights are compared over the same time period. On the basis of analyses of the 4-year dataset and comparisons between the platforms, several conclusions are reached.

1) At the ARM NSA site, all three CFs show the same general trend of increasing to an early spring maximum before subsequently decreasing in June, then rising to a secondary maximum in late summer and early fall with annual averages of 81.6%, 77.0%, and 66.0% for ARM, CC, and CERES-MODIS, respectively. The 5% CF difference between ARM and CC is mainly due to the CC measurement limitation in detecting clouds below 1 km. The CERES-MODIS CFs agree well with ARM and CC results during warm months (May-October), but are significantly lower during cold months (November-April). Therefore, it is concluded that the passive CERES-MODIS retrieved CFs agree well with those from CC and ARM during warm months, but the CERES Edition 3 polar cloud detection algorithms have

trouble distinguishing thin clouds from cold surface temperatures present during winter when only infrared data can be used.

2) Monthly means of CERES-MODIS H_{eff} over the ARM NSA site remain nearly constant, close to the cloud center, and basically fall within the cloud boundaries of ARM and CC measurements with an annual average of 3.2±2.3 km. The ARM and CC H_{top} means agree well during winter months and early spring, but start to deviate after April, when CC H_{top} continues to increase, whereas ARM H_{top} levels off or slightly decreases with a maximum difference between CC (7.3 km) and ARM (3.3 km) in September, which results from CC limitations in detecting clouds below 1 km and ARM radar-lidar limitations in measuring optically thin upper-level clouds, especially for multi-layered clouds. Cloud-base heights for both CC and ARM agree well, with a small difference of ~200 m.

3) Arctic-wide cloud fractions from CC during JJA are high, averaging to 77.1% for the season. CERES-MODIS retrievals over the same months show agreement with CC, deviating only ±10% across the majority of the Arctic. This agreement remains consistent across the Greenland and Barents Seas in DJF, where the warm currents from the Atlantic Ocean keep the area free of sea ice. However, across the remainder of the Arctic, CERES-MODIS underestimates CF by as much as 59%, indicating that the infrared techniques used in retrieving CERES-MODIS cloud properties over snow and ice surfaces struggle to capture accurate cloud fractions during polar night.

Differences in H_{top} and H_{eff} during JJA exceed those present during DJF. The PDFs and CDFs of H_{top} and H_{eff} during the winter months show that CERES-MODIS

cloud retrievals agree well in the lowest levels, as well as above an altitude of 9 km, leading to similarities in the DJF cloud heights. During JJA, however, CC detects a much higher frequency of clouds above 14 km that are likely optically thin cirrus clouds that CERES-MODIS algorithms cannot detect. The PDF of JJA cloud heights shows a higher frequency of low and mid-level CERES-MODIS cloud heights, indicating that these might be instances of multi-layer clouds, where CC detects the highest cloud layer, and CERES-MODIS detects the lowest, resulting in similar cloud fractions, but much different cloud heights.

4) Cloud fractions during the Antarctic summer average to 76.1%, with the highest CFs measured by CC over the surrounding oceans, and the lowest over the East Antarctic Ice Sheet. CERES-MODIS results agree well with CC over the ocean and coastal regions, typically remaining within 10% of CC retrievals. Over the East Antarctic Ice Sheet, however, CERES-MODIS struggles, underestimating CFs during December and January, but overestimating CFs in February. Through JJA, CFs from CC are slightly lower than those measured in DJF, but CERES-MODIS again shows underestimates of 20-30% in cold-season CFs.

Cloud heights from CC in DJF are low across the Antarctic, typically ranging between 5 and 8 km. CERES-MODIS H_{eff} values are similar, showing deviations of no more than ±3km. H_{top} values during JJA increase significantly with averages reaching higher than 12 km across the Antarctic land mass. Vertical distributions of cloud heights during these months show that CC distributions are more spread out than CERES-MODIS, with a relative maximum in occurrence at an altitude of 19.5 km. This percentage of clouds detected by CC at high altitudes, coupled with higher CC cloud

fractions during the JJA season, suggest that CC is detecting polar stratospheric clouds that are beyond the detection limits of the CERES-MODIS instruments.

5) CERES-MODIS retrieved cloud microphysical properties agree well with ARM retrievals during the summer months when the surface is free of snow and ice. The introduction of snow and ice below the cloud layers results in a significant disagreement in averages for τ and r_e between the surface and satellite retrievals. However, the average LWPs agree relatively well with the surface because of compensating errors. The optical depths retrieved from Aqua, which uses the 2.1 μm channel instead of the 1.6 μm near-infrared channel used by Terra, are underestimated too much because of errors in the retrieval input. These large discrepancies over snow surfaces may be due, in large part, to the presence of ice in the stratus clouds. These effects will need to be examined in detail to determine how they affect the retrievals and how they may be taken into account in future retrievals.

Future Work

The main focus of this study was to evaluate CERES-MODIS Edition 3 cloud property retrievals across the complicated terrain of polar regions. In the time that has passed since this project began, a fourth edition of CERES-MODIS cloud property retrievals has been produced, with distribution of these products expected to begin in the fall of 2012. Once this product has been released, a similar study of cloud fractions and cloud heights should be conducted to evaluate the new algorithms.

CERES-MODIS products include many cloud properties, including effective cloud particle phase, sizes, liquid and ice water paths, and cloud optical depths.

Investigating these cloud properties across the expanses of the Arctic and Antarctic, rather than in a localized region, will allow for a better understanding of any discrepancies that might be detected between the passive sensor onboard CERES-MODIS and the active sensors on CloudSat and CALIPSO.

While it is possible that these analyses will be used as references for the evaluation of other data sets, the main focus of this study was to show the areas where CERES-MODIS cloud retrievals in the Arctic and Antarctic struggle the most, and where they perform the best. It is the hope that this study will offer insight into the areas that need future improvement within CERES-MODIS retrievals, possibly leading to algorithms with the ability to more accurately depict polar cloud scenarios in the future.

REFERENCES

Adhikari, L., Z. Wang, and M. Deng (2012), Seasonal variations of Antarctic clouds observed by CloudSat and CALIPSO satellites, *J. Geophys. Res., 117*, D04202, doi:10.1029/2011JD016719.

Adhikari, L., Z. Wang, and D. Liu (2010), Microphysical properties of Antarctic polar stratospheric clouds and their dependence on tropospheric cloud systems, *J. Geophys. Res., 115*, D00H18, doi:10.1029/2009JD012125.

Bromwich, D. H., et al. (2012), Tropospheric clouds in Antarctica, *Rev. Geophys., 50*, RG1004, doi:10.1029/2011RG000363.

Carslaw, K. S., B. P. Luo, S. L. Clegg, Th. Peter, P. Briblecombe, P. J. Crutzen (1994), Stratospheric aerosol growth and HNO_3 gas phase depletion from coupled HNO_3 and water uptake by liquid particles, *Geophys. Res. Lett., 21(23)*, 2479-2482.

Cheremisin, A. A., A. V. Kushnarenko, V. N. Marichev, S. V. Nikolashkin, and P. V. Novikov (2007), Meteorological conditions and polar stratospheric clouds over Yakutsk in Winter 2004/05, *Russian Meteorology and Hydrology, 32(3)*, 176-182.

Chiriaco, M., et al. (2007), Comparison of CALIPSO-like, LaRC, and MODIS retrievals of ice cloud properties over SIRTA in France and Florida during CRYSTAL-FACE, *J. Appl. Meteorol. Climatol., 46(3)*, 249-272.

Clothiaux, E. E., T. P. Ackerman, G. G. Mace, K. P. Moran, R. T. Marchand, M. A. Miller, and B. E. Martner (2000), Objective determination of cloud heights and radar reflectivities using a combination of active remote sensors at the ARM CART sites, *J. Appl. Meteor., 39(5)*, 645-665.

Curry, J. A., et al (2000), FIRE Arctic Clouds Experiment, *Bull. Amer. Meteor. Soc.,* 81, 5-29.

Curry, J. A., J. L. Schramm, W. B. Rossow, and D. Randall (1996), Overview of Arctic cloud and radiation characteristics, *J. Climate, 9(8)*, 1731-1764.

Dong, X., T. P. Ackerman, and E. E. Clothiaux (1998), Parameterizations of the microphysical and shortwave radiative properties of boundary layer stratus from ground-based measurements, *J. Geophys. Res., 103*, 31681-31693.

Dong, X., and G. G. Mace (2003), Arctic stratus cloud properties and radiative forcing derived from ground-based data collected at Barrow, Alaska, *J. Climate, 16*, 445-461.

Dong, X., G. G. Mace, P. Minnis, and D. F. Young (2001), Arctic stratus cloud properties and their effect on the surface radiation budget: Selected cases from FIRE ACE, *J. Geophys. Res., 106*, 15297-15312.

Dong, X., P. Minnis, T. P. Ackerman, E. E. Clothiaux, G. G. Mace, C. N. Long, and J. C. Liljegren (2000), A 25-month database of stratus cloud properties generated from ground-based measurements at the Atmospheric Radiation Measurement Southern Great Plains Site, *J. Geophys. Res., 105*, 4529-4537, doi:10.1029/1999JD901159.

Dong, X., P. Minnis, G. G. Mace, W. L. Smith Jr, M. Poellot, R. Marchand, and A. Rapp (2002), Comparison of stratus cloud properties deduced from surface, GOES, and aircraft data during the March 2000 ARM Cloud IOP, *J. Atmos. Sci., 59*, 3265-3284.

Dong, X., P. Minnis, and B. Xi (2005), A climatology of midlatitude continental clouds from the ARM SGP Central Facility: Part I: Low-level cloud macrophysical, microphysical, and radiative properties, *J. Climate, 18(9)*, 1391-1410, doi:10.1175/JCLI3342.1.

Dong, X., P. Minnis, B. Xi, S. Sun-Mack, and Y. Chen (2008), Comparison of CERES-MODIS stratus cloud properties with ground-based measurements at the DOE ARM Southern Great Plains site, *J. Geophys. Res., 113*, D03204, doi:10.1029/2007JD008438.

Dong, X., B. Xi, K. Crosby, C. N. Long, R. S. Stone, and M. D. Shupe (2010), A 10-year climatology of Arctic cloud fraction and radiative forcing at Barrow, Alaska, *J. Geophys. Res., 115*, D17212, doi:10.1029/2009JD013489.

Han, Q., W. B. Rossow, and A. A. Lacis (1994), Near-global survey of effective droplet radii in liquid water clouds using ISCCP data, *J. Climate, 7*, 465-497.

Im, E., C. Wu, and S. L. Durden (2005), Cloud profiling radar for the CloudSat mission, *Aerospace and Electronic Systems Magazine, IEEE, 20(10)*, 15-18.

Intrieri, J. M., M. D. Shupe, T. Uttal, and B. J. McCarty (2002), An annual cycle of Arctic cloud characteristics observed by radar and lidar at SHEBA, *J. Geophys. Res., 107*, 8030, doi:10.1029/2000JC000423.

Kato, S., N. G. Loeb, P. Minnis, J. A. Francis, T. P. Charlock, D Rutan, E. E. Clothiaux, and S. Sun-Mack (2006), Seasonal and interannual variations of top-of-atmosphere irradiance and cloud cover over polar regions derived from the CERES data set, *Geophys. Res. Lett., 33*, L19804, doi:10.1029/2006GL026685.

Kato, S., S. Sun-Mack, W. F. Miller, F. G. Rose, Y. Chen, P. Minnis, and B. A. Wielicki (2010), Relationships among cloud occurrence frequency, overlap, and effective thickness derived from CALIPSO and CloudSat merged cloud vertical profiles, *J. Geophys. Res., 115,* D00H28, doi:10.1029/2009JD012277.

Kay, J. E., and A. Gettelman (2009), Cloud influence on and response to seasonal Arctic sea ice loss, *J. Geophys. Res., 114*, D18204, doi:10.1029/2009JD011773.

Liljegren, J. C., E. E. Clothiaux, G. G. Mace, S. Kato, and X. Dong (2001), A new retrieval for cloud liquid water path using a ground-based microwave radiometer and measurements of cloud temperature, *J. Geophys. Res., 106*, 14485-14500.

Liu, Y., S. A. Ackerman, B. C. Maddux, J. R. Key, and R. A. Frey (2010), Errors in cloud detection over the Arctic using a satellite imager and implications for observing feedback mechanisms, *J. Climate,23(7),* 1894-1907, doi:10.1175/2009JCLI3386.1.

McFarquhar, G. M., S. Ghan, J. Verlinde, A. Korolev, et al. (2011), Indirect and Semi-Direct Aerosol Campaign, the impact of Arctic aerosols on clouds, *Bull. Amer. Meteorol. Soc.*, 92, 183-201.

Minnis, P., et al. (2007), Evaluation of CERES-MODIS cloud properties using CALIPSO and CloudSat data, paper presented at A-Train Lille 07 Symposium, Lille Grand Palais, France.

Minnis, P., et al. (2008), Cloud detection in non-polar regions for CERES using TRMM VIRS and Terra and Aqua MODIS data, *IEEE Trans. Geosci. Remote Sens., 46*, 3857-3884.

Minnis, P., et al. (2010), CERES Edition 3 cloud retrievals, *Proc. AMS 13th Conf. Atmos. Rad.*, Portland, OR, June 27-July 2, 5.4.

Minnis, P., et al. (2011a), CERES Edition-2 cloud property retrievals using TRMM VIRS and Terra and Aqua MODIS Data—Part I: Algorithms, *Geosci. Remote Sens., 49,* 4374-4400.

Minnis P., et al. (2011b), CERES Edition-2 cloud property retrievals using TRMM VIRS and Terra and Aqua MODIS data—Part II: Examples of average results and comparisons with other data, *IEEE Trans. Geosci. Remote Sens., 49*, 4401-4430.

Moran, K. P., B. E. Martner, M. J. Post, R. A. Kropfli, D. C. Welsh, and K. B. Widener (1998), An unattended cloud-profiling radar for use in climate research, *Bull. Amer. Meteor. Soc.,79(3),* 443-455.

Noel, V., and M. Pitts (2012), Gravity wave events from mesoscale simulations, compared to polar stratospheric clouds observed from spaceborne lidar over the Antarctic Peninsula, *J. Geophys. Res., 117*, D11207, doi:10.1029/2011JD017318.

Pitts. M. C., Thomason, L. W., Poole, L. R., and Winker, D. M. (2007), Characterization of polar stratospheric clouds with spaceborne lidar: CALIPSO and the 2006 Antarctic season, *Atmos. Chem. Phys., 7*, 5207-5228.

Pitts., M. C., L. R. Poole, and L. W. Thomason (2009), Studies of PSC coverage and composition using CALIOP data, *CALIPSO/CloudSat Science Team Meeting*, Madison, WI, July 28-31.

Platnick, S., M. D. King, S. A. Ackerman, W. P. Menzel, B. A. Baum, J. C. Riedi, and R. A. Frey (2003), The MODIS cloud products: algorithms and examples from Terra, *Trans. Geosci. Remote Sens., 41(2)*, 459-473.

Platnick, S., J. Y. Li, M. D. King, H. Gerber, and P. V. Hobbs (2001), A solar reflectance method for retrieving the optical thickness and droplet size of liquid water clouds over snow and ice surfaces, *J. Geophys. Res., 106*, 15185-15199, doi:10.1029/2000JD900441.

Poole, L. R. and M. P. McCormick (1988), Polar stratospheric clouds and the Antarctic ozone hole, *J. Geophys. Res., 93(D7)*, 8423-8430.

Santee, M. L., et al. (2002), A Lagrangian approach to studying Arctic polar stratospheric clouds using UARS MLS HNO_3 and POAM II aerosol extinction measurements, *J. Geophys. Res., 107*, 4098, doi:10.1029/2000JD000227.

Shupe, Matthew D., et al. (2011), Clouds at Arctic atmospheric observatories. Part I: Occurrence and macrophysical properties, *J. Appl. Meteor., 50*, 626-644.

Spangenberg, D. A., Q. Trepte, P. Minnis, and T. Uttal (2004), Daytime cloud property retrievals over the Arctic from multispectral MODIS data, *Proc. 13th AMS Conf. Satellite Oceanogr. and Meteorol.*, Norfolk, VA, Sept. 20-24, CD-ROM, P7.11.

Steele, H. M., P. Hamill, M. P. McCormick, and T. J. Swissler (1983), The formation of Polar stratospheric clouds, *J. Atmos. Sci., 40*, 2055-2067.

Stephens, G. L., et al. (2002), The CloudSat mission and the A-Train, *Bull. Amer. Meteor. Soc., 83(12)*, 1771-1790.

Stephens, G. L., et al. (2008), CloudSat mission: Performance and early science after the first year of operation, *J. Geophys. Res., 113*, D00A18, doi:10.1029/2008JD009982.

Stetzer, O., O. Mohler, R. Wagner, S. Benz, H. Saathoff, H. Bunz, and O. Indris (2006), Homogeneous nucleation rates of nitric acid dehydrate (NAD) at simulated stratospheric conditions – Part 1: Experimental results, *Atmos. Chem. Phys., 6,* 3023-3033.

Stokes, G. M., and S. E. Schwartz (1994), The Atmospheric Radiation Measurement (ARM) Program: Programmatic background and design of the cloud and radiation test bed, *Bull. Amer. Meteor. Soc., 75(7),* 1201-1221.

Toon, O. B. and R. P. Turco (1991), Polar stratospheric clouds and ozone depletion, *Science American,* June, 68-74.

Trepte, Q., P. Minnis, and R. F. Arduini (2002), Daytime and nighttime polar cloud and snow identification using MODIS data. *Proc. SPIE 3rd Intl. Asia-Pacific Environ. Remote Sensing Symp., 2002: Remote Sens. Of Atmosphere, Ocean, Environment, and Space,* Hangzhou, China, October 23-27, Vol. 4891, 449-459.

Uttal, T., et al. (2002), Surface heat budget of the Arctic Ocean, *Bull. Amer. Meteor. Soc., 83(2),* 255-275.

Verlinden, K., D. W. J. Thompson, and G. L. Stephens (2011), The three-dimensional distribution of clouds over the Southern Hemisphere high latitudes, *J. Climate, 24,* 5799-5811.

Voigt, C., et al. (2000), Nitric Acid Trihydrate (NAT) in polar stratospheric clouds, *Science, 290,* 1756-1758.

Waibel, et al. (1999), Arctic ozone loss due to denitrification, *Science, 283,* 2064-2069.

Walden, V.P., and Coauthors (2001), The South Pole Atmospheric Radiation and Cloud Lidar Experiment (SPARCLE), Proc. Sixth Conf. on Polar Meteorology and Oceanography, San Diego, CA, Amer. Meteor. Soc., 297-299.

Wang, Z., G. Stephens, T. Deshler, C. Trepte, T. Parish, D. Vane, D. Winkler, D. Liu, and L. Adhikari (2008), Association of Antarctic polar stratospheric cloud formation on tropospheric cloud systems, *Geophys. Res. Lett., 35,* L13806, doi:10.1029/2008GL034209.

Wielicki, B. A., et al. (1998), Clouds and the Earth's Radiant Energy System (CERES): Algorithm overview, *Trans. Geosci. Remote Sens., 36(4),* 1127-1141.

Wielicki, B. A., B. R. Barkstrom, E. F. Harrison, R. B. Lee, G. Louis Smith, and J. E. Cooper (1996), Clouds and the Earth's Radiant Energy System (CERES): an earth observing system experiment, *Bull. Amer. Meteor. Soc., 77(5),* 853-868.

Winker, D. M., W. H. Hunt, and M. J. McGill (2007), Initial performance assessment of CALIOP, *Geophys. Res. Lett., 34(19),* L19803, doi:10.1029/2007GL030135.